NSWC TR 85-304

AN EDDY-CURRENT MODEL FOR THREE-DIMENSIONAL NONDESTRUCTIVE EVALUATION OF ADVANCED COMPOSITES

BY   HAROLD A. SABBAGH, L. DAVID SABBAGH, AND THOMAS M. ROBERTS (SABBAGH ASSOCIATES, INC.)

FOR   NAVAL SURFACE WEAPONS CENTER
RESEARCH AND TECHNOLOGY DEPARTMENT

28 JULY 1985

DTIC
ELECTE
MAY 2 1986

A

NAVAL SURFACE WEAPONS CENTER

Dahlgren, Virginia 22448-5000 ● Silver Spring, Maryland 20903-5000

86 5 1 007

REPORT DOCUMENTATION PAGE	READ INSTRUCTIONS BEFORE COMPLETING FORM

1. REPORT NUMBER	2. GOVT ACCESSION NO.	3. RECIPIENT'S CATALOG NUMBER
NSWC TR 85-304	AD-A167688	

4. TITLE *(and Subtitle)*	5. TYPE OF REPORT & PERIOD COVERED
AN EDDY-CURRENT MODEL FOR THREE-DIMENSIONAL NONDESTRUCTIVE EVALUATION OF ADVANCED COMPOSITES	Final; 11/28/84-7/28/85
	6. PERFORMING ORG. REPORT NUMBER SA/TR-1/85

7. AUTHOR(s)	8. CONTRACT OR GRANT NUMBER(s)
Harold A. Sabbagh L. David Sabbagh Thomas M. Roberts	N60921-85-C-0046

9. PERFORMING ORGANIZATION NAME AND ADDRESS	10. PROGRAM ELEMENT, PROJECT, TASK AREA & WORK UNIT NUMBERS
Sabbagh Associates, Inc. 2634 Round Hill Lane Bloomington, IN 47401	

11. CONTROLLING OFFICE NAME AND ADDRESS	12. REPORT DATE
Naval Surface Weapons Center, White Oak Code R34 Silver Spring, MD 20910	28 July 1985
	13. NUMBER OF PAGES 65

14. MONITORING AGENCY NAME & ADDRESS*(If different from Controlling Office)*	15. SECURITY CLASS. *(of this report)*
	UNCLASSIFIED
	15a. DECLASSIFICATION/DOWNGRADING SCHEDULE

16. DISTRIBUTION STATEMENT *(of this Report)*

Approved for public release; distribution unlimited.

17. DISTRIBUTION STATEMENT *(of the abstract entered in Block 20, if different from Report)*

18. SUPPLEMENTARY NOTES

19. KEY WORDS *(Continue on reverse side if necessary and identify by block number)*

Eddy-currents
Nondestructive Evaluation
Advanced Composites
Graphite-Epoxy

Electromagnetic Modeling
Electromagnetic Inverse Problems

20. ABSTRACT *(Continue on reverse side if necessary and identify by block number)*

This report describes work done by Sabbagh Associates, Inc. under contract N60921-85-C-0046 with the Naval Surface Weapons Center, White Oak, as part of the Center's Small Business Innovation Research Program (SBIR). The research problem is to develop a model and an inversion algorithm that is suitable for the three-dimensional quantitative nondestructive evaluation (NDE) of advanced composite materials by using eddy-currents. The approach

(20) (cont.)

is based on Sabbagh Associates' work in eddy-current NDE of conventional
metals. The technical objectives are to determine the feasibility of using
multifrequencies for this job, to determine in localized regions the fiber-
resin ratio in graphite epoxy, and to determine more precisely the types of
anomalies, whether flaws, delaminations, broken fibers, etc., that can be
reconstructed by our inversion method. These objectives are met by: (1)
applying rigorous electromangetic theory to determine a Green's function for
a slab of anisotropic composite material, (2)determining the integral relations
for the direct and inverse problems, using the Green's function just derived,
(3) determining suitable numerical algorithms for solving the inverse
problem, and (4) writing a computer program to execute the model. These
objectives have been met; in addition we illustrate some interesting electro-
magnetic phenomena in composite materials.

FOREWORD

This report describes work done by Sabbagh Associates, Inc. under contract N60921-85-C-0046 with the Naval Surface Weapons Center, White Oak, as part of the Center's Small Business Innovation Research Program (SBIR). The research problem is to develop a model and an inversion algorithm that is suitable for the three-dimensional quantitative nondestructive evaluation (NDE) of advanced composite materials by using eddy-currents. The approach is based on Sabbagh Associates' work in eddy-current NDE of conventional metals. The technical objectives are to determine the feasibility of using multifrequencies for this job, to determine in localized regions the fiber-resin ratio in graphite epoxy, and to determine more precisely the types of anomalies, whether flaws, delaminations, broken fibers, etc., that can be reconstructed by our inversion method. These objectives are met by: (1) applying rigorous electromagnetic theory to determine a Green's function for a slab of anisotropic composite material, (2) determining the integral relations for the direct and inverse problems, using the Green's function just derived, (3) determining suitable numerical algorithms for solving the inverse problem, and (4) writing a computer program to execute the model. These objectives have been met; in addition we illustrate some interesting electromagnetic phenomena in composite materials.

Composite materials in the form of fiber-reinforced matrix materials as, for example, graphite-epoxy, are being increasingly used in critical structures and structural components because of their high strength-to-weight ratio. Such structures range from high-performance aircraft to rocket motor cases to consumer goods, such as automobiles, golf clubs and tennis rackets. In order to assess the integrity of these structures, thereby determining the presence and size of flaws, it is necessary to employ suitable methods of quantitative nondestructive evaluation, such as eddy-currents. This research will have significant applications in the military and commercial aircraft industries, as well as automobiles and consumer products.

Approved by:

JACK R. DIXON, Head
Materials Branch

CONTENTS

ILLUSTRATIONS

ILLUSTRATIONS (Cont.)

TABLES

CHAPTER 1

IDENTIFICATION AND SIGNIFICANCE OF THE PROBLEM

The proposed research problem is to develop a model and an inversion algorithm that is suitable for the quantitative nondestructive evaluation (NDE) of advanced composite materials by using electromagnetic methods, especially eddy-currents. We are specifically interested in determining, in localized regions, the fiber-resin ratio in graphite-epoxy.

Composite materials in the form of fiber-reinforced matrix materials as, for example, graphite-epoxy, are being increasingly used in critical structures and structural components because of their high strength-to-weight ratio. In order to assess the integrity of these structures, it is necessary to employ suitable methods for quantitative NDE. One method uses eddy-currents; composite materials, however, are inherently anisotropic, which means that many of the classical eddy-current technology and design procedures are not applicable. In addition, composite materials vary widely in their permittivities and conductivities, which means that new analyses must be carried out to develop effective strategies for using eddy-currents in quantitative NDE. A final problem is that there is a variety of potential failure modes in composites, such as delaminations, fiber-breakage due to impact damage, flaws, etc., some of which may not be readily detectable by eddy-currents [1]. In order to complement the empirical studies of [1] it is necessary to embark upon a rigorous quantitative NDE program for composites to assess the role that eddy-currents play in it, and especially to determine a suitable inversion algorithm.

In quantitative NDE one seeks to determine the orientation and spatial extent of flaws, i.e., to reconstruct or image flaws. By so quantifying a flaw one is better able to assess its potential for damaging the structure in which it is located, thereby offering a means for judging whether to eliminate the flawed member or not. Clearly, such decisions can save hundreds of thousands of dollars in "down time", as well as potentially saving lives.

The present state of the art in quantitative eddy-current NDE of composites does not include the ability to reconstruct or image anomalous regions, or flaws, in three dimensions. The objective of Phase I research, therefore, is to develop a model and algorithm suitable for inverting eddy-current data for the reconstruction of flaws in quantitative NDE of advanced composite materials. The specific technical objectives are:

1. To develop a model describing the interaction of induced eddy-currents and the conducting graphite fibers in graphite epoxy,

2. To develop a fiber density algorithm based on this model,

3. To determine the feasibility of using multifrequencies for this job.

These objectives can be met by accomplishing the following:

1. Apply rigorous electromagnetic theory to determine a Green's function for a stratified half-space, or a finite slab, of anisotropic composite materials.

2. Determine the integral relations for the direct and inverse problem, using the Green's function derived in 1.

3. Determine suitable numerical algorithms for solving the inverse problem.

4. Write a computer program to execute the model.

Electromagnetic theory and the Green's function are dealt with in Chapters 2–4, and in Appendices A, B and C. Integral equations for the direct and inverse problems are derived in Chapter 5, which also includes a discussion of the discretization of these equations by means of the method of moments and the use of multifrequencies. Chapter 6 describes the numerical algorithms that were used: these are least-squares, by means of the singular value decomposition and QR-decomposition, together with the Levenberg-Marquardt stabilization parameter, and an iterative algorithm for analytic continuation (or Fourier extrapolation.)

We conclude the report with a description of some numerical experiments, comments and conclusions.

CHAPTER 2

AN ELECTROMAGNETIC MODEL FOR GRAPHITE-EPOXY

BACKGROUND

Eddy-current methods for the examination of carbon fiber reinforced epoxy resins and other composite materials have been discussed and analyzed by Owston and Prakash [2]-[5]. These analyses have been based on an *ad hoc* equivalent circuit in which the composite test piece is regarded as being inductively coupled to the probe, much as in the classical treatment of eddy-current evaluation of metals. Though the technique gives a useful indication of the form of the results, a more satisfactory approach, as Owston [4] points out, is to use a field-theoretic analysis which is capable of giving exact results for a given model. A field-theoretic analysis is also desirable when computing electromagnetic interactions for shielding effectiveness of advanced composites in aircraft [6].

The heart of the problem is to determine a Green's function for the composite material. (The Green's function is the electromagnetic field produced by a point-source of current.) Much work has been done in recent years on the subject of electromagnetic interactions with composite materials, mostly in the context of electromagnetic shielding of avionics equipment from electromagnetic pulses [6]-[10]. Some of this work is directly applicable to the problem of computing eddy-current flow within composites, but the Green's function problem must be attacked by applying rigorous electromagnetic theory to anisotropic media.

CONSTITUTIVE RELATIONS FOR ADVANCED COMPOSITES

Advanced composite materials are laminates made up of a number of individual layers bonded together. Each layer consists of a unidirectional array of long fibers embedded in, and firmly bonded to, a matrix. The basic building blocks of any specific composite are defined by the types of fibers and matrix involved. Some fiber-matrix systems are: boron-epoxy, graphite-epoxy, Kevlar-epoxy, graphite-polymide and graphite-thermoplastic [7].

The matrix for each of these materials is normally a good dielectric, whereas the fibers vary in electrical conductivity from modest (graphite) to a poor dielectric (boron) to a good dielectric (Kevlar). These materials are nonmagnetic, so that the magnetic permeability is μ_0.*

Composites have anisotropic conductivities because of the unidirectional arrays of fibers within. For example, for graphite-epoxy the average macroscopic conductivity along the fiber direction is 20,000 mhos/m, whereas in the direction transverse to the fibers, the conductivity is 100 mhos/m. It may be surprising to find a nonzero transverse conductivity

---

* These, and other facts about electromagnetic constitutive relations, are taken from [7], which is the most complete reference on electromagnetic modeling of composite materials that we have found.

in graphite-epoxy, in view of the earlier statement that the matrix is a good dielectric. The fact is that there is enough local fiber-to-fiber contact that the average macroscopic conductivity is not zero. (See Figure 1(a).) Other materials, of course, have different longitudinal and transverse conductivities, as shown in Table 1 [7]:

TABLE 1.   SUMMARY OF ELECTRICAL PROPERTIES
OF SOME COMPOSITES

	Graphite-Epoxy	Boron-Epoxy	Kevlar
Permeability μ_R	1	1	1
Permittivity ϵ_R	indeterminate	5.6	3.6
DC Conductivity (mhos/m)			
longitudinal σ_L	2×10^4	30	6×10^{-9}
transverse σ_T	100	2×10^{-8}	6×10^{-9}
Anisotropy Ratio (σ_L/σ_T)	200	1.5×10^9	1

The reason that ϵ_R for graphite-epoxy is indeterminate is because the fiber-to-fiber contact effectively shunts the capacitance between fibers with a fairly low resistance path, making it impossible to measure dielectric permittivities at frequencies less than 100 megahertz, or so. Thus, in Figure 1(b), which shows a possible ac equivalent circuit for eddy-current flow, the capacitors are effectively shorted by the fiber-to-fiber resistors at the lower frequencies.

The anisotropy of the composite manifests itself in a complex permittivity tensor, the tensor being diagonal in a coordinate system (ξ_1, ξ_2, ξ_3), where ξ_1 is parallel to the average fiber direction, ξ_2 is perpendicular to the average fiber direction, but lies in the plane of the composite layer, and ξ_3 is perpendicular to both fibers and the plane of the layer:

$$\bar{\bar{\epsilon}} = \begin{pmatrix} \hat{\epsilon}_{11} & 0 & 0 \\ 0 & \hat{\epsilon}_{22} & 0 \\ 0 & 0 & \hat{\epsilon}_{33} \end{pmatrix}. \tag{1}$$

Here, $\hat{\epsilon}_{ii} = \epsilon_{ii} - j\frac{\sigma_{ii}}{\omega}$, with $j = \sqrt{-1}$, and ω is the angular frequency. The coordinate system just defined, for which the complex permittivity tensor is diagonal, is not necessarily the laboratory coordinate system, (x, y, z), in which the electromagnetic field vectors are defined. In any case, the tensor symbol will be used, and the components in a particular coordinate system may be computed by applying the usual rules for transforming Cartesian tensors.

From here on we will consider only graphite-epoxy, for which $\epsilon_{11} = \epsilon_{22} = \epsilon_{33} = \epsilon_0$, $\sigma_{11} = 2 \times 10^4$ mhos/m, and $\sigma_{22} = \sigma_{33} = 100$ mhos/m.

MATRIX WAVE EQUATIONS FOR GRAPHITE-EPOXY

Maxwell's equations are the fundamental equations for electromagnetic analysis. Using the constitutive relations just defined for graphite-epoxy, these equations become, in

the sinusoidal steady-state:

$$\nabla \times \overline{E} = -j\omega\mu_0\overline{H}$$

$$\nabla \times \overline{H} = j\omega\overline{\overline{\epsilon}} \cdot \overline{E} + \overline{J}^{(i)}. \tag{2}$$

Because of the anisotropy of graphite-epoxy, it is convenient to work with a matrix formulation of these equations that has been useful in crystal optics, plasmas and microwave devices [11]-[19]. We start by writing (2) in the 6×6 matrix form

$$\begin{pmatrix} j\omega\overline{\overline{\epsilon}} & -\nabla \times \overline{\overline{I}} \\ \nabla \times \overline{\overline{I}} & j\omega\mu_0\overline{\overline{I}} \end{pmatrix} \begin{pmatrix} \overline{E} \\ \overline{H} \end{pmatrix} = \begin{pmatrix} -\overline{J}^{(i)} \\ \overline{0} \end{pmatrix}, \tag{3}$$

where the permittivity tensor includes a conductivity term, as in (1), except that the matrix is not necessarily diagonal. $\overline{\overline{I}}$ is the identity matrix, and $\overline{0}$ is the zero vector.

We write the matrix of partial derivatives as:

$$\begin{pmatrix} \overline{\overline{0}} & -\nabla \times \overline{\overline{I}} \\ \nabla \times \overline{\overline{I}} & \overline{\overline{0}} \end{pmatrix} = \overline{\overline{U}}_1 \, \partial/\partial x + \overline{\overline{U}}_2 \, \partial/\partial y + \overline{\overline{U}}_3 \, \partial/\partial z, \tag{4}$$

where

$$\overline{\overline{U}}_1 = \begin{pmatrix} \overline{\overline{0}} & \begin{matrix} 0 & 0 & 0 \\ 0 & 0 & 1 \\ 0 & -1 & 0 \end{matrix} \\ \begin{matrix} 0 & 0 & 0 \\ 0 & 0 & -1 \\ 0 & 1 & 0 \end{matrix} & \overline{\overline{0}} \end{pmatrix}, \qquad \overline{\overline{U}}_2 = \begin{pmatrix} \overline{\overline{0}} & \begin{matrix} 0 & 0 & -1 \\ 0 & 0 & 0 \\ 1 & 0 & 0 \end{matrix} \\ \begin{matrix} 0 & 0 & 1 \\ 0 & 0 & 0 \\ -1 & 0 & 0 \end{matrix} & \overline{\overline{0}} \end{pmatrix},$$

$$\overline{\overline{U}}_3 = \begin{pmatrix} \overline{\overline{0}} & \begin{matrix} 0 & 1 & 0 \\ -1 & 0 & 0 \\ 0 & 0 & 0 \end{matrix} \\ \begin{matrix} 0 & -1 & 0 \\ 1 & 0 & 0 \\ 0 & 0 & 0 \end{matrix} & \overline{\overline{0}} \end{pmatrix}. \tag{5}$$

When these matrices are substituted into (3), along with the definitions

$$\bar{e} = \begin{pmatrix} \overline{E} \\ \overline{H} \end{pmatrix}, \quad \bar{j}^{(i)} = \begin{pmatrix} \overline{J}^{(i)} \\ \overline{0} \end{pmatrix}, \quad \overline{\overline{K}} = \begin{pmatrix} \overline{\overline{\epsilon}} & \overline{\overline{0}} \\ \overline{\overline{0}} & \mu_0\overline{\overline{I}} \end{pmatrix}, \tag{6}$$

we get

$$\left[j\omega\overline{\overline{K}} + \overline{\overline{U}}_1 \, \partial/\partial x + \overline{\overline{U}}_2 \, \partial/\partial y + \overline{\overline{U}}_3 \, \partial/\partial z \right] \bar{e} = -\bar{j}^{(i)}. \tag{7}$$

Upon defining the two-dimensional Fourier transforms in (x,y) by

$$\tilde{\bar{e}}(k_x, k_y, z) = \frac{1}{4\pi^2} \iint_{-\infty}^{\infty} \bar{e}(x,y,z) e^{j(k_x x + k_y y)} \, dx \, dy \tag{8}(a)$$

$$\bar{e}(x,y,z) = \iint_{-\infty}^{\infty} \tilde{\bar{e}}(k_x, k_y, z) e^{-j(k_x x + k_y y)} \, dk_x \, dk_y, \tag{8}(b)$$

5

we take the Fourier transform of (7):

$$\left[j\omega\overline{\overline{K}} - jk_x\overline{\overline{U}}_1 - jk_y\overline{\overline{U}}_2 + \overline{\overline{U}}_3\, d/dz\right]\tilde{\tilde{e}} = -\tilde{\tilde{j}}^{(i)}. \tag{9}$$

To get this result we assume that the composite material is homogeneous in the (x,y) plane, so that $\overline{\overline{K}}$ is independent of (x,y).

The third and sixth rows of (9) are independent of z-derivatives. Thus, we can use these two equations to solve for $\tilde{e}_3$ and $\tilde{e}_6$ in terms of the remaining variables:

$$\tilde{e}_3 = -\frac{K_{31}}{K_{33}}\tilde{e}_1 - \frac{K_{32}}{K_{33}}\tilde{e}_2 + \frac{k_y}{\omega K_{33}}\tilde{e}_4 - \frac{k_x}{\omega K_{33}}\tilde{e}_5 - \frac{\tilde{j}_3^{(i)}}{j\omega K_{33}} \tag{10}(a)$$

$$\tilde{e}_6 = -\frac{k_y}{\omega\mu_0}\tilde{e}_1 + \frac{k_x}{\omega\mu_0}\tilde{e}_2 \quad . \tag{10}(b)$$

When we use these two equations to eliminate the z-components from the remaining equations in (9) we end up with system of four first-order differential equations in the four transverse electromagnetic field components. This system is written as the 4×4 vector-matrix equation:

$$\frac{d\tilde{\tilde{e}}_t}{dz} = \overline{\overline{S}}\,\tilde{\tilde{e}}_t + \overline{\overline{U}}\,\tilde{\tilde{j}}^{(i)}, \tag{11}$$

where

$$\tilde{\tilde{e}}_t = [\tilde{e}_1, \tilde{e}_2, \tilde{e}_4, \tilde{e}_5] = \left[\tilde{E}_x, \tilde{E}_y, \tilde{H}_x, \tilde{H}_y\right]; \tag{12}$$

the subscript, 't', denotes transverse field variables.

The components of $\overline{\overline{S}}$ and $\overline{\overline{U}}$ are:

$$S_{11} = \frac{jk_x K_{31}}{K_{33}}, \qquad S_{12} = \frac{jk_x K_{32}}{K_{33}}, \qquad S_{13} = \frac{-jk_x k_y}{\omega K_{33}}, \qquad S_{14} = -j\omega\mu_0 + j\frac{k_x^2}{\omega K_{33}}$$

$$S_{21} = \frac{jk_y K_{31}}{K_{33}}, \qquad S_{22} = \frac{jk_y K_{32}}{K_{33}}, \qquad S_{23} = j\omega\mu_0 - j\frac{k_y^2}{\omega K_{33}}, \qquad S_{24} = j\frac{k_x k_y}{\omega K_{33}}$$

$$S_{31} = j\omega K_{21} - j\omega\frac{K_{23}K_{31}}{K_{33}} + j\frac{k_x k_y}{\omega\mu_0}, \qquad S_{32} = j\omega K_{22} - j\omega\frac{K_{23}K_{32}}{K_{33}} - j\frac{k_x^2}{\omega\mu_0}$$

$$S_{33} = \frac{jk_y K_{23}}{K_{33}}, \qquad S_{34} = \frac{-jk_x K_{23}}{K_{33}}, \qquad S_{41} = -j\omega K_{11} + j\omega\frac{K_{13}K_{31}}{K_{33}} + j\frac{k_y^2}{\omega\mu_0}$$

$$S_{42} = -j\omega K_{12} + j\omega\frac{K_{13}K_{32}}{K_{33}} - j\frac{k_x k_y}{\omega\mu_0}, \qquad S_{43} = \frac{-jk_y K_{13}}{K_{33}}, \qquad S_{44} = \frac{jk_x K_{13}}{K_{33}}$$

$$\tag{13}$$

$$U_{11} = 0, \qquad U_{12} = 0, \qquad U_{13} = \frac{k_x}{\omega K_{33}}$$

$$U_{21} = 0, \qquad U_{22} = 0, \qquad U_{23} = \frac{k_y}{\omega K_{33}}$$

$$U_{31} = 0, \qquad U_{32} = 1, \qquad U_{33} = -\frac{K_{23}}{K_{33}}$$

$$U_{41} = -1, \qquad U_{42} = 0, \qquad U_{43} = \frac{K_{13}}{K_{33}}. \tag{14}$$

CHAPTER 3

DERIVATION OF A GREEN'S FUNCTION FOR A GRAPHITE-EPOXY SLAB

The formal solution of (11) defines the Green's function, $\widetilde{\overline{\overline{G}}}$:

$$\tilde{e}_t(z) = \int \widetilde{\overline{\overline{G}}}(z|z') \cdot \tilde{j}^{(i)}(z') dz'. \tag{15}$$

The double bars over G denote a tensor, and the tilde over any variable means a transverse Fourier transform, as before. Clearly, the Green's function is the transverse field at z due to a point current source at z'. Thus, it is a 4×3 tensor, because there are four transverse field components, as shown in (12), and the point current source can be oriented in the x-, y-, or z-direction. Because the current flow in the models studied in this report are confined to the transverse plane, i.e., the (x,y)-plane, we will be interested in only the first two columns of $\widetilde{\overline{\overline{G}}}$.

The calculation of the Green's function requires a knowledge of the eigenmodes of (11) for a nonstratified medium. These are solutions of the homogeneous form of (11), with $\overline{\overline{S}}$ constant with respect to z. The eigenmode theory is developed in Appendix A.

In order to compute $\widetilde{\overline{\overline{G}}}$ we must know the geometry of the composite material. In this report we will work with the plane-parallel slab that is shown in Figure 2, with the x-axis parallel to the fiber direction, and the y-direction transverse. Thus, the region of interest consists of three parts: the region above the slab (which is free space), the composite slab, and the region below the slab. Call these regions 1, 2, 3, respectively, as shown in Figure 2, and introduce the following notation for the Green's function:

$$\widetilde{\overline{\overline{G}}}_{ij}(z|z') = \text{Field produced at } z \text{ in region } i, \text{ due to a}$$
$$\text{point source of current at } z' \text{ in region } j;$$
$$i,j = 1,2,3.$$

As we will see later, the only Green's functions that are needed are $\widetilde{\overline{\overline{G}}}_{21}$ and $\widetilde{\overline{\overline{G}}}_{12}$.

In order to compute $\widetilde{\overline{\overline{G}}}_{21}$, consider Figure 3(a), in which the point-source of current is located at z' in region 1. We further subdivide the three regions into four regions, called A-D, and expand the vector field solutions in each of these four regions in terms of the eigenvectors of Appendix A:

$$A: \quad a \begin{pmatrix} -\alpha_{10} \\ -\alpha_{20} \\ 0 \\ 1 \end{pmatrix} e^{-\lambda_0(z-z')} + b \begin{pmatrix} 0 \\ -\beta_{10} \\ 1 \\ -\beta_{20} \end{pmatrix} e^{-\lambda_0(z-z')} \tag{16)(a}$$

$$B: \quad c \begin{pmatrix} \alpha_{10} \\ \alpha_{20} \\ 0 \\ 1 \end{pmatrix} e^{\lambda_0(z-z')} + d \begin{pmatrix} -\alpha_{10} \\ -\alpha_{20} \\ 0 \\ 1 \end{pmatrix} e^{-\lambda_0(z-z')} + e \begin{pmatrix} 0 \\ \beta_{10} \\ 1 \\ -\beta_{20} \end{pmatrix} e^{\lambda_0(z-z')}$$

$$+ f \begin{pmatrix} 0 \\ -\beta_{10} \\ 1 \\ -\beta_{20} \end{pmatrix} e^{-\lambda_0(z-z')} \quad (16)(b)$$

$$C: \quad c' \begin{pmatrix} \alpha_1 \\ \alpha_2 \\ 0 \\ 1 \end{pmatrix} e^{\lambda_1 z} + d' \begin{pmatrix} -\alpha_1 \\ -\alpha_2 \\ 0 \\ 1 \end{pmatrix} e^{-\lambda_1 z} + e' \begin{pmatrix} 0 \\ \beta_1 \\ 1 \\ -\beta_2 \end{pmatrix} e^{\lambda_3 z} + f' \begin{pmatrix} 0 \\ -\beta_1 \\ 1 \\ -\beta_2 \end{pmatrix} e^{-\lambda_3 z} \quad (16)(c)$$

$$D: \quad g \begin{pmatrix} \alpha_{10} \\ \alpha_{20} \\ 0 \\ 1 \end{pmatrix} e^{\lambda_0(z+z_0)} + h \begin{pmatrix} 0 \\ \beta_{10} \\ 1 \\ -\beta_{20} \end{pmatrix} e^{\lambda_0(z+z_0)}, \quad (16)(d)$$

where $\alpha_1 = S_{14}/\lambda_1$, $\alpha_2 = S_{24}/\lambda_1$, $\beta_1 = \lambda_3/S_{32}$, and $\beta_2 = S_{31}/S_{32}$. The subscript '0' denotes quantities defined in isotropic free-space.

Equations 16(a) and 16(d) contain only outgoing waves at $\pm$infinity. In order to determine the unknown expansion coefficients a through h, c' through f', we must satisfy certain boundary conditions. The fields must be continuous at the two boundaries, $z = 0$, and $z = -z_0$, which do not contain current singularities. At $z = -z'$, which does contain a point singularity, there must be a discontinuity. The amount of discontinuity can be inferred from (11), in which the imposed source current has the form:

$$\bar{j}^{(i)} = \hat{j} \, e^{j k_z z'} e^{j k_y y'} \delta(z - z'), \quad (17)$$

where $\hat{j}$ is the unit vector in the direction of current flow.

Upon integrating (11) an infinitesimal distance across the plane $z = z'$, we get

$$\bar{e}_t^{(+)} - \bar{e}_t^{(-)} = \overline{\overline{U}} \hat{j} \, e^{j k_z z'} e^{j k_y y'}, \quad (18)$$

where $(+)$ denotes the limit immediately above z', and $(-)$ denotes the limit immediately below.

In order to find the response to x-directed currents (the first column of the Green's tensor) we let $\hat{j} = \bar{a}_x$. The right-hand side of (18) becomes

$$\begin{pmatrix} 0 \\ 0 \\ 0 \\ -1 \end{pmatrix} e^{j k_z z'} e^{j k_y y'}. \quad (19)$$

Similarly, for a y-directed current, which will produce the second column of the Green's tensor, we let $\vec{j} = \bar{a}_y$, and get

$$\begin{pmatrix} 0 \\ 0 \\ 1 \\ 0 \end{pmatrix} e^{jk_x x'} e^{jk_y y'} \tag{20}$$

for the right-hand side of (18).

Once we obtain the boundary conditions, the solution for the expansion coefficients becomes a straight-forward problem in linear algebra.

The computation of $\widetilde{\overline{\overline{G}}}_{12}$ proceeds in a similar manner, except that the four subregions are shifted downward, as shown in Figure 3(b). The field expansions are given by:

$$A: \quad a \begin{pmatrix} -\alpha_{10} \\ -\alpha_{20} \\ 0 \\ 1 \end{pmatrix} e^{-\lambda_0 z} + b \begin{pmatrix} 0 \\ -\beta_{10} \\ 1 \\ -\beta_{20} \end{pmatrix} e^{-\lambda_0 z} \tag{21)(a}$$

$$B: \quad c \begin{pmatrix} \alpha_1 \\ \alpha_2 \\ 0 \\ 1 \end{pmatrix} e^{\lambda_1(z+z')} + d \begin{pmatrix} -\alpha_1 \\ -\alpha_2 \\ 0 \\ 1 \end{pmatrix} e^{-\lambda_1(z+z')} + e \begin{pmatrix} 0 \\ \beta_1 \\ 1 \\ -\beta_2 \end{pmatrix} e^{\lambda_3(z+z')}$$
$$+ f \begin{pmatrix} 0 \\ -\beta_1 \\ 1 \\ -\beta_2 \end{pmatrix} e^{-\lambda_3(z+z')} \tag{21)(b}$$

$$C: \quad c' \begin{pmatrix} \alpha_1 \\ \alpha_2 \\ 0 \\ 1 \end{pmatrix} e^{\lambda_1(z+z')} + d' \begin{pmatrix} -\alpha_1 \\ -\alpha_2 \\ 0 \\ 1 \end{pmatrix} e^{-\lambda_1(z+z')} + e' \begin{pmatrix} 0 \\ \beta_1 \\ 1 \\ -\beta_2 \end{pmatrix} e^{\lambda_3(z+z')}$$
$$+ f' \begin{pmatrix} 0 \\ -\beta_1 \\ 1 \\ -\beta_2 \end{pmatrix} e^{-\lambda_3(z+z')} \tag{21)(c}$$

$$D: \quad g \begin{pmatrix} \alpha_{10} \\ \alpha_{20} \\ 0 \\ 1 \end{pmatrix} e^{\lambda_0(z+z_0)} + h \begin{pmatrix} 0 \\ \beta_{10} \\ 1 \\ -\beta_{20} \end{pmatrix} e^{\lambda_0(z+z_0)}, \tag{21)(d}$$

and the current singularity is at z', which is within the slab.

The boundary conditions, including the discontinuity condition, (18), are the same as before. In particular, the inhomogeneous terms, (19) and (20), corresponding to an x-directed and y-directed current source, respectively, continue to hold.

In Appendix B we sketch the application of the boundary conditions for solving for the expansion coefficients for $\tilde{\bar{\bar{G}}}_{12}$. The process for $\tilde{\bar{\bar{G}}}_{21}$ is similar. After the coefficients have been determined, we substitute c' through f' into (16)(c) to complete the computation of $\tilde{\bar{\bar{G}}}_{21}$; for $\tilde{\bar{\bar{G}}}_{12}$ we substitute (a, b) into (21)(a). These steps complete the solution of the Green's tensor.

CHAPTER 4

CALCULATION OF THE ELECTROMAGNETIC FIELD
WITHIN A GRAPHITE-EPOXY SLAB

Having computed a Green's function for the graphite-epoxy slab, it is possible to determine the field within the slab due to currents above the slab (by using $\overline{\overline{\widetilde{G}}}_{21}$), or to determine the field above the slab due to currents within the slab (by using $\overline{\overline{\widetilde{G}}}_{12}$). The latter operation will be used in the inverse problem. The method of determining the fields, given the currents, is to use (15).

We have considered four different impressed current sources, $\widetilde{\overline{j}}^{(i)}$: an infinite current sheet, a filamentary circular current loop, and two finite circular current sheets with distributed windings, one with a uniform distribution, and the other with a linearly increasing distribution. Each of the current sources is parallel to the surface of the slab. The three circular currents simulate, to a degree, flat 'pancake' coils.

The infinite current sheet plays a significant role in the inversion process, which will be presented in the next two chapters, and will be discussed first.

INFINITE CURRENT SHEET

The problem is illustrated in Figure 4. In the Fourier transform domain, the current sheet is given by

$$\widetilde{\overline{j}}^{(i)}(k_x, k_y, z') = I_0\delta(k_x)\delta(k_y)\delta(z' - z'')(\bar{a}_x \cos\theta + \bar{a}_y \sin\theta), \qquad (22)$$

where I_0 is the surface current density in amperes per meter, and θ is the direction of current flow. The delta function at the origin of (k_x, k_y) space is due to the fact that the current sheet is uniform over the entire (x, y) plane. The principal axes are the x- and y-axes, the x-axis being along the fiber direction, and the y-axis transverse. We will compute the field within the slab when the current is oriented along either of these axes (i.e., $\theta = 0°$ or $90°$) , and then use a simple tensor transformation to compute the fields when the current sheet is oriented at any other angle.

Because the spectrum of $\widetilde{\overline{j}}^{(i)}$ is concentrated at the origin, we can simply put $k_x = k_y = 0$ in computing the Green's function, $\overline{\overline{\widetilde{G}}}_{21}$. Of course, the evaluation of the integral in (15) is simplified because of the delta function at z''. These facts allow us to write down a simple analytic expression for the transverse fields within the slab:

current in x-direction:

$$\begin{pmatrix} \widetilde{E}_x \\ \widetilde{E}_y \\ \widetilde{H}_x \\ \widetilde{H}_y \end{pmatrix} = c' \begin{pmatrix} -\eta_{11} \\ 0 \\ 0 \\ 1 \end{pmatrix} e^{\lambda_1 z} + d' \begin{pmatrix} \eta_{11} \\ 0 \\ 0 \\ 1 \end{pmatrix} e^{-\lambda_1 z}; \qquad (23)(a)$$

11

current in y-direction:

$$\begin{pmatrix} \widetilde{E}_x \\ \widetilde{E}_y \\ \widetilde{H}_x \\ \widetilde{H}_y \end{pmatrix} = e' \begin{pmatrix} 0 \\ \eta \\ 1 \\ 0 \end{pmatrix} e^{\lambda_3 z} + f' \begin{pmatrix} 0 \\ -\eta \\ 1 \\ 0 \end{pmatrix} e^{-\lambda_3 z}, \qquad (23)(b)$$

where

$$c' = g\left(\frac{\eta_{11} + \eta_0}{2\eta_{11}}\right)e^{\lambda_1 z_0}, \qquad d' = g\left(\frac{\eta_{11} - \eta_0}{2\eta_{11}}\right)e^{-\lambda_1 z_0}$$

$$g = \frac{e^{-\lambda_0 z''}}{2\alpha_{11}} I_0$$

$$\alpha_{11} = \frac{(\eta_{11} + \eta_0)^2 e^{\lambda_1 z_0} - (\eta_{11} - \eta_0)^2 e^{-\lambda_1 z_0}}{(\eta_{11} + \eta_0)^2 - (\eta_{11} - \eta_0)^2}$$

$$e' = h\left(\frac{\eta + \eta_0}{2\eta}\right)e^{\lambda_3 z_0}, \qquad f' = h\left(\frac{\eta - \eta_0}{2\eta}\right)e^{-\lambda_3 z_0} \qquad (24)$$

$$h = \frac{-e^{-\lambda_0 z''}}{2\alpha_{22}} I_0$$

$$\alpha_{22} = \frac{(\eta + \eta_0)^2 e^{\lambda_3 z_0} - (\eta - \eta_0)^2 e^{-\lambda_3 z_0}}{(\eta + \eta_0)^2 - (\eta - \eta_0)^2}$$

$$\lambda_0 = j\omega(\mu_0\epsilon_0)^{1/2}, \lambda_1 = j\omega(\mu_0 K_{11})^{1/2}, \lambda_3 = j\omega(\mu_0 K)^{1/2},$$

$$\eta_0 = (\mu_o/\epsilon_0)^{1/2}, \eta_{11} = (\mu_0/K_{11})^{1/2}, \eta = (\mu_0/K)^{1/2}.$$

We see from (23) that an x-directed uniform current sheet produces an x-directed electric field and a y-directed magnetic field, whereas a y-directed current sheet produces a y-directed electric field and an x-directed magnetic field. This is what we expect from an isotropic medium; it occurs in an anisotropic medium when the x- and y-directions are principal axes for the medium.

For an "off-axis" orientation of the current sheet, however, the results are much different and must be calculated by using a simple tensor transformation. Let T_{xx} and T_{yy} be the electric fields produced within the slab due to a current sheet above the slab. Then in the principal coordinate system, (x, y), we have

$$\begin{pmatrix} \widetilde{E}_x \\ \widetilde{E}_y \end{pmatrix} = \begin{pmatrix} T_{xx} & 0 \\ 0 & T_{yy} \end{pmatrix} \begin{pmatrix} \widetilde{j}_x^{(i)} \\ \widetilde{j}_y^{(i)} \end{pmatrix}, \qquad (25)$$

so that

$$\begin{pmatrix} \widetilde{J}_x \\ \widetilde{J}_y \end{pmatrix} = \begin{pmatrix} \sigma_{11} T_{xx} & 0 \\ 0 & \sigma T_{yy} \end{pmatrix} \begin{pmatrix} \widetilde{j}_x^{(i)} \\ \widetilde{j}_y^{(i)} \end{pmatrix}. \qquad (26)$$

Let (x', y') be the rotated coordinate system. Then

$$\begin{pmatrix} x' \\ y' \end{pmatrix} = \begin{pmatrix} \cos\theta & \sin\theta \\ -\sin\theta & \cos\theta \end{pmatrix} \begin{pmatrix} x \\ y \end{pmatrix}. \qquad (27)$$

12

Hence, the relationship between the induced current and the exciting current, in the (x', y') coordinate system, is

$$
\begin{pmatrix} \tilde{J}_{x'} \\ \tilde{J}_{y'} \end{pmatrix} = \begin{pmatrix} \cos\theta & \sin\theta \\ -\sin\theta & \cos\theta \end{pmatrix} \begin{pmatrix} \tilde{J}_x \\ \tilde{J}_y \end{pmatrix} \tag{28}
$$

$$
= \begin{pmatrix} \cos\theta & \sin\theta \\ -\sin\theta & \cos\theta \end{pmatrix} \begin{pmatrix} \sigma_{11}T_{xx} & 0 \\ 0 & \sigma T_{yy} \end{pmatrix} \begin{pmatrix} \cos\theta & -\sin\theta \\ \sin\theta & \cos\theta \end{pmatrix} \begin{pmatrix} \tilde{j}_{x'}^{(i)} \\ \tilde{j}_{y'}^{(i)} \end{pmatrix}
$$

$$
= \begin{pmatrix} \sigma_{11}T_{xx}\cos^2\theta + \sigma T_{yy}\sin^2\theta & (-\sigma_{11}T_{xx} + \sigma T_{yy})\sin\theta\cos\theta \\ (-\sigma_{11}T_{xx} + \sigma T_{yy})\sin\theta\cos\theta & \sigma_{11}T_{xx}\sin^2\theta + \sigma T_{yy}\cos^2\theta \end{pmatrix} \begin{pmatrix} \tilde{j}_{x'}^{(i)} \\ \tilde{j}_{y'}^{(i)} \end{pmatrix}.
$$

The magnitudes of the currents that are induced at the surface of the slab are plotted in Figure 5(a), for a frequency of 10^6 Hz, and $\sigma_{11} = 2 \times 10^4$, $\sigma = 100$. The slab thickness, z_0, is 1.27 cm (0.5 inches), and z'', the height of the current sheet above the slab, is 2.54 mm (0.1 inch). We assume that the current sheet carries current in the x' direction only; the angular variable shown in Figure 5(a) is the angle between the x' and x axes. Now we see that, generally, there is a component of current (the smaller loop) that flows transverse to the direction of the current sheet. The larger curve is the component of current that flows parallel to the exciting current. For an isotropic medium, the smaller loop would vanish, and the larger curve would be an arc of a circle.

These results are in qualitative agreement with those of Prakash and Owston [3], who used a simple theoretical analysis that was based on an equivalent circuit. We can extend the field model that has been developed in this report to include slabs that consist of graphite-epoxy laminates of differing "lay-up order", i.e., in which the laminates have their principal axes differing from one-another. In addition, we can include the effects of non-simple excitation sources, such as the "horse-shoe" eddy-current probe of Prakash and Owston [3]. An advantage of the more extensive field-theoretic analysis is that it more clearly suggests the limits of simpler equivalent circuit models.

CIRCULAR CURRENT DISTRIBUTIONS

The circular currents produce more interesting field distributions than does the infinite current sheet. Expressions for $\tilde{j}^{(i)}(k_x, k_y, z)$ for each of the distributions are derived in Appendix C. We note, now, that the spectrum of each current distribution is no longer concentrated at the origin, so that we must compute $\tilde{\overline{\overline{G}}}_{21}$ for all k_x, k_y, as described in Chapter 3. When $\tilde{\overline{\overline{G}}}_{21}$ and $\tilde{j}^{(i)}$ are substituted into (15), we obtain the transverse Fourier transform of the transverse field vector at any level, z, within the slab. Then, upon taking the inverse Fourier transform, say by using the Fast Fourier Transform (FFT) algorithm, we get the fields in physical space, at each level, z. We have done this for each of the current distributions, and have found that the results are qualitatively similar in all three cases; hence, we will display results of the filamentary loop, only. The parameters, dimensions and frequency are the same as for the current sheet; the radius of the current loop is 0.5 inch (1.27 cm).

Before going into the anisotropic problem, we illustrate, in Figure 5(b), the fields induced into an isotropic medium (with conductivity 2×10^4 mhos/m) at a depth of 0.05 inch (0.127 cm). The isotropic nature of the response is clearly apparent; if we were to look vertically downward we would see a circular response region. Each pixel is a square, whose side is 0.05 inch. Thus, the response region has a diameter of about 1.0 inch, which is the diameter of the current loop. Therefore, the result agrees with our intuition.

The situation in an anisotropic material is changed dramatically, however. In this case the fibers will 'guide' the field, so that it will die out much less rapidly in the x-direction (along the fibers) than in the y-direction. This is illustrated quite clearly in Figure 5(c), where the complex values of the x- and y-components of the electric field at a depth of 0.05 inch are shown. The response region in this figure is highly elongated in the x-direction, when viewed from directly above. The x-component of the induced electric current field is obtained by multiplying the x-component of the electric field by σ_{11}, which is equal to 2×10^4 mhos/m, and the y-component of the current is given by the product of the y-component of electric field with σ_{22} (100 mhos/m). Therefore, the eddy-currents do not flow in the usual circular paths of an unbounded isotropic medium, as suggested by Figure 5(b), but, rather, flow in highly elongated quasi-elliptical paths. The degree of eccentricity of the paths depends upon the degree of anisotropy, as measured by the ratio, σ_{11}/σ_{22}.

In many applications it is important to know how rapidly the induced field dies out with depth into the slab. In an anisotropic medium there is no unique skin-depth, because the conductivity varies with direction of the electric field. Therefore, the problem must be handled numerically in most cases. We present in Figure 5(d) model calculations of the induced electric field at a depth of 0.4 inches within the slab. The excitation source is the filamentary current loop of before, and the frequency remains 1 MHz. Upon comparing this figure with Figure 5(c), we draw the following conclusions: the field magnitude is reduced by about an order-of-magnitude, the field is much more spread out in the y-direction and is very uniform in the x-direction. These results are consistent with the notion of diffusion in isotropic media; they are an obvious manifestation of the filtering-out of the higher spatial frequencies, k_x, k_y, with depth, and the crowding of the spatial-frequency spectrum toward the origin. In addition, we note that the x-component of the electric field dies out much more rapidly with depth than does the y-component. This is due to the fact that in the principal axis coordinate system the x-component interacts with a much larger conductivity, σ_{11}, than does the y-component (which interacts with σ_{22}.) This supports our statement that there is no unique skin-depth in graphite-epoxy.

Model computations of the type presented in this chapter can be very useful in setting up eddy-current experiments in graphite-epoxy, and interpreting the results.

CHAPTER 5

INTEGRAL EQUATIONS FOR THE DIRECT AND INVERSE PROBLEMS

DIRECT AND INVERSE PROBLEMS

At this point we introduce some systems-related ideas that should make clearer the way our concept of inversion is used for nondestructive evaluation. Refer to Figure 6, which shows a "system", together with its input and output. In part (a) of the figure the input is known and so is the system, and the output is to be determined. This is the "forward" or "direct" problem. For example, the input could be current or voltage source and the system, a coil coupled to the composite workpiece. The output, the electromagnetic field or induced eddy-current within the workpiece, can be directly computed in a straightforward manner by electromagnetic theory; we have done this in Chapter 4, by computing the eddy-current induced into the workpiece as a function of the orientation of the exciting current-sheet.

In part (b) the system and output are known, and the input is to be determined. This is a problem of communication theory, or signal detection. One assumes a catalog of possible input signals to be available, whose structure and characteristics are known *a priori*; from the known output one estimates the input signal on the basis of the maximum *a posteriori* probability of its occurrence.

This is the basis of the application of feature extraction and artificial intelligence to nondestructive evaluation. It is an example of another forward method, and appears to be sufficient for many applications. It is, however, limited by both the large volume of signal waveforms that must be catalogued for a suitable generalized interpretation and by the subjective comparisons made by the interpreter. The method also gives little indication of the sensitivity of the solution to possible errors in the data and the degree of non-uniqueness associated with the chosen model.

In Figure 6(c) both the input and output are known and the system is unknown. The input could be a known probing signal and the output, the measured response to the probe. The object is to determine the nature of the system.

This is an example of system identification, or parameter estimation, where "parameter" refers to certain parameters of the unknown system. In the sense that problems (a) and (b) are direct, problem (c) is the "indirect" or "inverse" problem, and is the problem attacked in this research effort. What one seeks in this problem is a model-system that, when operating on the input, produces a model-output that is, in some sense, an optimum estimate of the known output.

In Figure 7 we show a current-sheet that excites a region of the composite workpiece, and a sensor that measures the scattered field. Within the workpiece lies an anomalous region (the "flaw") that we wish to reconstruct. A mathematical mesh is defined that surrounds the anomaly, as shown. The system, then, consists of the current-sheet, the sensor, the workpiece, and the mesh that encloses the anomalous region. The unknown

parameters that are to be estimated in order that the system be identified, in the sense of Figure 6(c) and the discussion about it, are the generalized electrical permittivities that are to be assigned to each cell of the mesh. The known input is the current to the current-sheet, and the known outputs are the field components at the sensor. Clearly, if we can determine the permittivity map that is defined on the mesh, we will have reconstructed the anomalous region.

The method of solving this problem is based on minimizing the square of the error between the actual measured data and that produced by the model-system, the model-output. The parameters that are varied to produce the optimum model, in the least squares sense, are, of course, the permittivities that are assigned to each cell in the mesh of Figure 7.

Thus, mathematically, we wish to determine a set of unknown parameters, $\{\epsilon_j\}$, $j = 1, \ldots, M$, where M is the number of cells in the mesh, from a set of data, $\{e_i\}$, $i = 1, \ldots, N$, where $\{e_i\}$ is the field component measured by the sensor at a number of points, and at a number of different frequencies (if we are using a multifrequency approach). The $\{e_i\}$ are functionally related to the $\{\epsilon_j\}$ in a known way:

$$
\begin{aligned}
e_1 &= f_1(\epsilon_1, \ldots, \epsilon_M) \\
&\vdots \\
e_N &= f_N(\epsilon_1, \ldots, \epsilon_M).
\end{aligned}
\tag{29}
$$

Hence, given the $\{\epsilon_j\}$, we can calculate the $\{e_i\}$ by treating this as a "forward" problem, in the sense of Figure 6(a).

It is the $\{e_i\}$, however, that are the given data, so we must invert the system, (29), to determine the $\{\epsilon_j\}$. We do this by minimizing the error function

$$
F(\epsilon_1, \ldots, \epsilon_M) = \left[\sum_{i=1}^{N} (e_i - f_i)^2 \right]^{1/2}.
\tag{30}
$$

Iterative methods are commonly used to carry out the minimization of (30). The iterative method successively improves a current model, i.e., a current estimate of the $\{\epsilon_j\}$, until the error measure, (30), is small and the parameters are stable with respect to reasonable changes in the model.

The equations that define the forward and inverse problems are integral equations that are determined by using electromagnetic theory; they will be derived next.

INTEGRAL RELATIONS FOR THE DIRECT AND INVERSE PROBLEMS

The detection of flaws, or anomalies, by means of eddy-currents depends upon the fact that flaws have different electrical parameters than the host material, and, therefore, the eddy-current flow is interrupted at the boundary of the flaw. The flaw, therefore,

can be considered to be an inhomogeneity, which consists of a tensor permittivity, $\bar{\bar{\epsilon}}_f$ that is imbedded in a region whose tensor permittivity, $\bar{\bar{\epsilon}}_0$, is known *a priori*. The magnetic permeability of each region is μ_0. Hence, Maxwell's equations for the two regions are:

$$\nabla \times \overline{E}_0 = -j\omega\mu_0\overline{H}_0 \qquad \text{known region}$$

$$\nabla \times \overline{H}_0 = j\omega\bar{\bar{\epsilon}}_0 \cdot \overline{E}_0 \tag{31}(a)$$

$$\nabla \times \overline{E}_f = -j\omega\mu_0\overline{H}_f \qquad \text{flawed region}$$

$$\nabla \times \overline{H}_f = j\omega\bar{\bar{\epsilon}}_f \cdot \overline{E}_f \tag{31}(b).$$

Upon subtracting (31)(b) from (31)(a), we get:

$$\nabla \times (\overline{E}_0 - \overline{E}_f) = -j\omega\mu_0(\overline{H}_0 - \overline{H}_f)$$
$$\nabla \times (\overline{H}_0 - \overline{H}_f) = j\omega\bar{\bar{\epsilon}}_0 \cdot (\overline{E}_0 - \overline{E}_f) + j\omega(\bar{\bar{\epsilon}}_0 - \bar{\bar{\epsilon}}_f) \cdot \overline{E}_f, \tag{32}$$

where we have added and subtracted $j\omega\bar{\bar{\epsilon}}_0 \cdot \overline{E}_f$ to get the final result.

Thus, the perturbation of the electromagnetic field, $\overline{E}_0 - \overline{E}_f$, $\overline{H}_0 - \overline{H}_f$, satisfies the same equation as the original electromagnetic field within the known region, except for the presence of the term $\overline{J}_a = j\omega(\bar{\bar{\epsilon}}_0 - \bar{\bar{\epsilon}}_f) \cdot \overline{E}_f$. This term, which is equivalent to a current source, represents the presence of the anomalous region, or flaw. It is important to note that this current source vanishes off of the flaw, because there the tensor permittivities are equal. Thus, we say that the anomalous current density has a "compact support"; it occupies a finite spatial extent.

Equation (32) has the same form as (2), with the anomalous current playing the role of the impressed current. Thus, (32) can be transformed into the transverse-matrix format, (11), whose solution is given by (15), again with the impressed current replaced by the anomalous current. The general form of the solution is

$$(\tilde{e}_0 - \tilde{e}_f)(z) = \int \tilde{\bar{\bar{G}}}(z|z') \cdot \tilde{j}_a(z')dz'. \tag{33}$$

We suppress the subscript, t, on the transverse field variable, $\tilde{e}$, to avoid confusion with other subscripts.

Before going further, we define:

$$\tilde{e}_{1,2}(z) = \text{transverse field in region 1 or 2,}$$
$$\text{with the flaw present}$$
$$\tilde{e}_0(z) = \text{transverse field with the flaw absent,}$$
$$\text{due to the exciting current sheet.}$$

With this notation, together with the corresponding notation for the Green's function in Chapter 3, we can use (33) to write down the following integral equation for computing the field within the flawed region, which is in region 2:

$$\tilde{e}_0(z) = \tilde{e}_2(z) + \int_{flaw} \tilde{\bar{\bar{G}}}_{22}(z|z') \cdot \tilde{j}_a(z')dz', \tag{34}(a)$$

17

where

$$\bar{J}_a = j\omega(\bar{\bar{\epsilon}}_0 - \bar{\bar{\epsilon}}_f) \cdot \overline{E}_2. \tag{34}(b)$$

The known field, $\tilde{\bar{e}}_0$, that appears in (34)(a) has already been calculated in Chapter 4.

Equations (34)(a),(b) are the integral equations for the direct problem: given the anomalous permittivity, $(\bar{\bar{\epsilon}}_0 - \bar{\bar{\epsilon}}_f)$, compute the field $\tilde{e}_2(z)$.

The integral equation for the inverse problem is also derived from (33), except now the fields on the left-hand side are in region 1, because they are measured by the sensor (recall Figure 7). The anomalous current is still in region 2, of course, so that we have:

$$(\tilde{\bar{e}}_0 - \tilde{\bar{e}}_1)(z) = \int_{flaw} \tilde{\bar{\bar{G}}}_{12}(z|z') \cdot \tilde{\bar{j}}_a(z')dz', \tag{35}$$

where $\bar{J}_a$ is defined as in (34)(b).

Equations (34) and (35) (or, more precisely, their discretized versions) constitute the model system that was discussed in (29) and (30). The rigorous algorithm for using the system consists of first computing the incident field, $\tilde{\bar{e}}_0$, at the flaw, by the methods of Chapter 4; this is the left-hand side of (34)(a). For a given distribution of flaw permittivity, $\bar{\bar{\epsilon}}_f(z)$, (34) can be solved numerically by the method of moments [20]. The solution of (34), $\tilde{\bar{e}}_2$, in the flawed region is the source term for (35), which produces the perturbed field at the sensor. This is the model field that is compared with the measured field to determine if the assumed flaw permittivity is "close" to the actual (though unknown) flaw permittivity. The problem is really nonlinear because (34) and (35) involve the product of two unknowns, the flaw permittivity and the electric field within the flaw. Thus, we resort to the iteration just outlined to get a solution. This iteration consists of a series of "direct" problems, which are the solution of (34), given an assumed flaw permittivity, and "inverse" problems, wherein we determine the flaw permittivity from (35), given the measured fields at the sensor.

A LINEARIZED INVERSE MODEL

This iteration is time consuming, so we seek a means of linearizing the problem. From some of our previous work in numerical electromagnetic modeling of two-dimensional flaws in conventional metals [30], together with laboratory results [31], we have found that we can approximate $\tilde{\bar{e}}_2$, that appears in (35), by the known field, $\tilde{\bar{e}}_0$, that is produced by the current sheet, and that has already been computed in Chapter 4. This linearizes the problem, decouples the inverse problem from the direct problem and, in fact, renders the solution of the direct problem unnecessary.

In the linearized approximation we have

$$
\begin{aligned}
\overline{J}_a(x,y,z) &\approx j\omega(\bar{\bar{\epsilon}}_0 - \bar{\bar{\epsilon}}_f) \cdot \overline{E}_0 \\
&= j\omega(\epsilon_0\bar{\bar{I}} - j\bar{\bar{\sigma}}_0/\omega - \epsilon_0\bar{\bar{I}} + j\bar{\bar{\sigma}}_f/\omega) \cdot \overline{E}_0 \\
&= (\bar{\bar{\sigma}}_0 - \bar{\bar{\sigma}}_f) \cdot \overline{E}_0 \\
&= \bar{\bar{\sigma}}_a \cdot \overline{E}_0.
\end{aligned} \tag{36}
$$

Note that the anomalous conductivity, $\bar{\bar{\sigma}}_a$, has a compact support in the (x,y) plane.

$\overline{E}_0$ is uniform in the (x,y) plane; hence, the transverse Fourier transform yields $\tilde{\bar{j}}_a(k_x, k_y, z) = \tilde{\bar{\bar{\sigma}}}_a(k_x, k_y, z) \cdot \overline{E}_0$, and when this is substituted into (35), we get the basic approximate integral equation for inversion:

$$\tilde{e}(\xi) = \int_{-z_0}^{0} \tilde{\bar{\bar{G}}}_{12}(\xi|z') \cdot \tilde{\bar{\bar{\sigma}}}_a(z') \cdot \overline{E}_0(z')dz', \tag{37}$$

where the left-hand side is the perturbed field measured by the sensor at $z = \xi$.

We assume that the anomalous conductivity tensor has the same structure (including the same principal axes) as the host conductivity tensor. Hence, in the principal axes, we have:

$$\tilde{\bar{\bar{\sigma}}}_a = \begin{pmatrix} \tilde{\sigma}_{a_{11}} & 0 & 0 \\ 0 & \tilde{\sigma}_{a_{22}} & 0 \\ 0 & 0 & \tilde{\sigma}_{a_{33}} \end{pmatrix}, \tag{38}$$

with $\tilde{\sigma}_{a_{22}} = \tilde{\sigma}_{a_{33}}$. Our host material satisfies $\sigma_{11} = 20,000$, $\sigma_{22} = \sigma_{33} = 100$ mhos/m.

We know from our work with the current sheet that an x-directed current induces an x-directed electric field, and a y-directed current induces a y-directed field (as long as we are in the principal-axes coordinate system). Hence,

$$\begin{aligned} \tilde{\bar{\bar{\sigma}}}_a(z') \cdot \overline{E}_0(z') &= \tilde{\sigma}_{a_{11}}(z')E_{01}(z')\bar{a}_x, \quad \text{if current is in x direction} \\ &= \tilde{\sigma}_{a_{22}}(z')E_{02}(z')\bar{a}_y, \quad \text{if current is in y direction.} \end{aligned} \tag{39}$$

DISCRETIZING THE INTEGRAL EQUATION

We discretize the integral equation for inversion by appealing to the method of moments, together with a multifrequency approach. In applying the method of moments we first divide the slab into N_z plane-parallel regions, and expand $\tilde{\sigma}_{a_{11}}$, and $\tilde{\sigma}_{a_{22}}$ in terms of pulse functions defined on this partition:

$$\tilde{\sigma}_{a_{11}}(k_x, k_y, z') = \sum_{j=1}^{N_z} \tilde{\sigma}_j^{11}(k_x, k_y)P_j(z'), \tag{40}$$

where

$$P_j(z') = \begin{cases} 1, & \text{if } z_j^{(-)} \le z' < z_j^{(+)} \\ 0, & \text{otherwise}, \end{cases}$$

and $z_j^{(-)}$, $z_j^{(+)}$ are, respectively, the bottom and top of the jth layer.

When this is substituted into (39), and that result into (37), we get

$$\begin{aligned} \tilde{e}(\xi) &= \sum_{j=1}^{N_z} \tilde{\sigma}_j^{11} \int_{z_j^{(-)}}^{z_j^{(+)}} \tilde{\bar{\bar{G}}}_{12}(\xi|z') \cdot \bar{a}_x E_{01}(z')dz', \quad \text{current in x direction} \\ &= \sum_{j=1}^{N_z} \tilde{\sigma}_j^{22} \int_{z_j^{(-)}}^{z_j^{(+)}} \tilde{\bar{\bar{G}}}_{12}(\xi|z') \cdot \bar{a}_y E_{02}(z')dz', \quad \text{current in y direction.} \end{aligned} \tag{41}$$

19

The dot product, $\widetilde{\overline{\overline{G}}} \cdot \bar{a}_x$, picks out the first column of $\widetilde{\overline{\overline{G}}}$, and $\widetilde{\overline{\overline{G}}} \cdot \bar{a}_y$ does the same for the second. Hence, upon letting $l(= 1, 2, 3, 4)$ stand for the lth row of $\widetilde{\overline{\overline{G}}}$, and suppressing the subscripts on $\widetilde{\overline{\overline{G}}}$, because we know that we are working with a source point in region 2 and field point in region 1, then (41) becomes

$$
\begin{aligned}
\tilde{e}_l(\xi) &= \sum_{j=1}^{N_z} \tilde{\sigma}_j^{11} \int_{z_j^{(-)}}^{z_j^{(+)}} \widetilde{G}_{l1}(\xi|z') E_{01}(z') dz', \quad \text{current in x direction} \\
&= \sum_{j=1}^{N_z} \tilde{\sigma}_j^{22} \int_{z_j^{(-)}}^{z_j^{(+)}} \widetilde{G}_{l2}(\xi|z') E_{02}(z') dz', \quad \text{current in y direction.}
\end{aligned}
\tag{42}
$$

This result is a discretization of the unknown conductivity distribution. We proceed by noting that the conductivity is independent of ω, whereas $\tilde{G}$ and E_0 are not. Hence, we can get a system of equations by using (42) at a number, N_f, of frequencies, $\{\omega_i\}$, $i = 1, \ldots, N_f$:

$$
\begin{aligned}
\tilde{e}_l(\omega_i) &= \sum_{j=1}^{N_z} \widetilde{H}_{ij}^{l1} \tilde{\sigma}_j, \quad \text{current in x direction} \\
&= \sum_{j=1}^{N_z} \widetilde{H}_{ij}^{l2} \tilde{\sigma}_j, \quad \text{current in y direction} \\
&\quad i = 1, \ldots, N_f.
\end{aligned}
\tag{43}
$$

The matrices are defined by:

$$
\begin{aligned}
\widetilde{H}_{ij}^{l(1,2)} &= \int_{z_j^{(-)}}^{z_j^{(+)}} \widetilde{G}_{l(1,2)}(\xi|z'; \omega_i) E_{0(1,2)}(z', \omega_i) dz' \\
&\quad i = 1, \ldots, N_f \\
&\quad j = 1, \ldots, N_z \\
&\quad l = 1, 2, 3, 4.
\end{aligned}
\tag{44}
$$

Normally, we will be interested in sensing the magnetic field, and not the electric. Thus, $l = 3, 4$ in (44), where '3' refers to the x component, and '4' to the y component of the magnetic field. Thus, we refer to the matrices in (44) as H_{ij}^{xx}, H_{ij}^{xy}, H_{ij}^{yx}, and H_{ij}^{yy}.

When the system matrices of (43) are nonsquare, as they will be if $N_f \neq N_z$, then least-squares methods are used to solve the problem. This model is called a "multifrequency model" because of the manner of acquiring data. The frequencies should be chosen so that the system matrix is reasonably well-conditioned in the mathematical sense, i.e., so that the columns of the matrix are relatively independent of each other. Putting it loosely, this reduces the ambiguity in deciding which layer contributes to the measured magnetic field. If we use a broad range of frequencies, for example, the system matrix will have a

structure that is approximated by Figure 8. The zeroes are not true zeroes but are numbers that are much smaller than the x's. This structure is due to the physical phenomenon of "skin-effect", wherein high-frequency eddy-currents are confined to the surface nearest the exciting source. The matrix of Figure 8, because it is roughly triangular, has reasonably independent columns.

We solve (43) for each spatial-frequency pair, (k_x, k_y), which gives us the Fourier transfrom of the unknown conductivity at each layer. Then we take the inverse Fourier transform of this solution vector to get the actual distribution of conductivity within the anomalous region.

CHAPTER 6

NUMERICAL ALGORITHMS FOR THE INVERSE PROBLEM

INTRODUCTION TO LEAST-SQUARES

The final step in the inversion process is to solve (43), which we rewrite in the vector-matrix form:

$$\overline{\overline{A}}\,\bar{x} = \bar{b}, \tag{45}$$

where $\bar{x}$ is the unknown vector, $\bar{b}$ the data vector and $\overline{\overline{A}}$ the $m \times n$ system matrix. We seek a least-squares solution, as defined next. Let the residual vector, $\bar{r}(\bar{x})$, be defined by:

$$\bar{r}(\bar{x}) = \bar{b} - \overline{\overline{A}}\,\bar{x}. \tag{46}$$

Upon introducing the usual squared-norm notation, we have:

$$\|\bar{r}(\bar{x})\| = \Big[\sum_{i=1}^{m} r_i^2(x_1,\ldots,x_n)\Big]^{1/2}. \tag{47}$$

Then the definition of a least-squares solution of (45) is: given $\bar{b} = (b_1,\ldots,b_m)$, find $\bar{x} = (x_1,\ldots,x_n)$ that minimizes $\|\bar{r}(\bar{x})\|$; i.e., solve

$$\min_{\bar{x}} \|\bar{b} - \overline{\overline{A}}\,\bar{x}\|. \tag{48}$$

If $\bar{x}^*$ is a solution of (48), then it is known that [21]

$$\overline{\overline{A}}^{\mathrm{H}}\bar{r}^* = \overline{\overline{A}}^{\mathrm{H}}(\bar{b} - \overline{\overline{A}}\,\bar{x}^*) = \bar{0}, \tag{49}$$

where the superscript, H, denotes the complex-conjugate transpose (or Hermitian transpose) of a matrix. Thus,

$$\overline{\overline{A}}^{\mathrm{H}}\overline{\overline{A}}\,\bar{x}^* = \overline{\overline{A}}^{\mathrm{H}}\bar{b}, \tag{50}$$

or

$$\bar{x}^* = \overline{\overline{A}}^{+}\bar{b}, \tag{51}$$

where $\overline{\overline{A}}^{+} = (\overline{\overline{A}}^{\mathrm{H}}\overline{\overline{A}})^{-1}\overline{\overline{A}}^{\mathrm{H}}$ is the pseudoinverse of $\overline{\overline{A}}$.

While (51) characterizes the mathematical solution of (48), we don't actually numerically compute $\overline{\overline{A}}^{+}$, because of the potential loss of precision. For numerical solutions other methods are used, namely, the QR-factorization and singular value decomposition (SVD), as described below. These two methods are also useful when $\overline{\overline{A}}$ has less than full rank, i.e., when its columns are not linearly independent.

LEVENBERG-MARQUARDT REGULARIZATION

It must be noted, now, that (45) is a model equation, whereas the data vector that is actually measured will contain uncertainties due to noise, quantizing error in analog-to-digital conversion, an imprecise model, etc. Due to this uncertainty in the data, therefore, we really have to deal with the following equation:

$$\overline{\overline{A}}\bar{x} + \bar{\eta} = \bar{b}, \tag{52}$$

where $\bar{\eta}$ is the data-uncertainty vector. If the norm of $\bar{\eta}$ is ϵ, then from (52) we want the norm of the residuals to satisfy:

$$\|\overline{\overline{A}}\bar{x} - \bar{b}\| \leq \epsilon. \tag{53}$$

Since $\overline{\overline{A}}$ is ill-conditioned (typical values of the condition number are $10^4 - 10^8$), the solution of (52) will be unstable, because of the data uncertainty. To help smooth the solution we impose a constraint on the norm of the solution:

$$\|\bar{x}\| \leq M. \tag{54}$$

Inequalities (53) and (54) can be combined to yield:

$$\|\overline{\overline{A}}\bar{x} - \bar{b}\|^2 + \left(\frac{\epsilon}{M}\right)^2 \|\bar{x}\|^2 \leq 2\epsilon^2. \tag{55}$$

Hence, our problem becomes: minimize the functional

$$F_\lambda(\bar{x}) = \|\overline{\overline{A}}\bar{x} - \bar{b}\|^2 + \lambda^2 \|\bar{x}\|^2, \tag{56}$$

where $\lambda = (\epsilon/M)$ is the Levenberg-Marquardt, or regularizing parameter.

The vector that minimizes (56) is

$$\bar{x} = (\overline{\overline{A}}^H \overline{\overline{A}} + \lambda^2 \overline{\overline{I}})^{-1}. \tag{57}$$

Thus, the presence of the Levenberg-Marquardt parameter modifies the pseudoinverse of $\overline{\overline{A}}$ in such a manner as to stabilize the solution. This will be seen again when we discuss the singular value decompostion next.

THE SINGULAR VALUE DECOMPOSITION

As before, we don't actually compute a modified pseudoinverse; instead, we work directly with $\overline{\overline{A}}$, augmented in a certain manner. Equation (57) is the solution of

$$(\overline{\overline{A}}^H \overline{\overline{A}} + \lambda^2 \overline{\overline{I}})\bar{x} = \overline{\overline{A}}^H \bar{b}, \tag{58}$$

which are the normal equations for the least-squares problem [22]:

$$\begin{pmatrix} \overline{\overline{A}} \\ \hline \lambda \overline{\overline{I}} \end{pmatrix} \bar{x} \cong \begin{pmatrix} \bar{b} \\ \hline \bar{0} \end{pmatrix}, \tag{59}$$

where $\cong$ denotes equality in the least-squares sense of minimizing a norm.

The solution of (59) is based on the singular value decomposition (SVD) [21,22] of $\overline{\overline{A}}$:

$$\overline{\overline{A}} = \overline{\overline{U}} \begin{pmatrix} \overline{\overline{S}} \\ \hline \overline{\overline{0}} \end{pmatrix} \overline{\overline{V}}^{\mathrm{H}}, \tag{60}$$

where $\overline{\overline{U}}(m \times m)$ and $\overline{\overline{V}}(n \times n)$ are unitary, and $\overline{\overline{S}} = \mathrm{diag}(s_1, \ldots, s_n)$; the $\{s_i\}$ are the singular values of $\overline{\overline{A}}$.

Letting

$$\bar{x} = \overline{\overline{V}} \bar{y} \tag{61}(a)$$

$$\bar{g} = \overline{\overline{U}}^{\mathrm{H}} \bar{b}, \tag{61}(b)$$

we get, from (59):

$$\begin{pmatrix} \overline{\overline{S}} \\ \hline \overline{\overline{0}} \\ \hline \lambda \overline{\overline{I}} \end{pmatrix} \bar{y} \cong \begin{pmatrix} \bar{g} \\ \hline \bar{0} \end{pmatrix} . \tag{62}$$

The $\lambda \overline{\overline{I}}$ term can be eliminated by using Givens rotations [21,22], with the result:

$$\begin{pmatrix} \overline{\overline{S}}^{(\lambda)} \\ \hline \overline{\overline{0}} \\ \hline \overline{\overline{0}} \end{pmatrix} \bar{y} \cong \begin{pmatrix} \bar{g}^{(\lambda)} \\ \hline \bar{h}^{(\lambda)} \end{pmatrix}, \tag{63}$$

where

$$g_i^{(\lambda)} = \begin{cases} g_i s_i / s_i^{(\lambda)}, & i = 1, \ldots, n \\ g_i, & i = n+1, \ldots, m \end{cases} \tag{64}(a)$$

$$h_i^{(\lambda)} = -g_i \lambda / s_i^{(\lambda)}, \qquad i = 1, \ldots, n \tag{64}(b)$$

$$\overline{\overline{S}}^{(\lambda)} = \mathrm{diag}(s_1^{(\lambda)}, \ldots, s_n^{(\lambda)}) \tag{64}(c)$$

$$s_i^{(\lambda)} = (s_i^2 + \lambda^2)^{1/2}, \qquad i = 1, \ldots, n. \tag{64}(d)$$

24

It is clear from (64)(d) that the Levenberg-Marquardt parameter accomplishes its stabilization role by increasing the size of the smallest singular values; it is these singular values that contribute to the ill-conditioning of the matrix.

From (63), therefore, we have

$$y_i = g_i s_i / (s_i^{(\lambda)})^2, \qquad i = 1, \ldots, n \tag{65}$$

which, from (61)(a), produces the final result:

$$\bar{x} = \sum_{i=1}^{n} [g_i s_i / (s_i^{(\lambda)})^2] \overline{V}_i, \tag{66}$$

where $\overline{V}_i$ is the ith column vector of $\overline{\overline{V}}$.

An excellent computer code for computing the singular value decomposition is ZSVDC in the LINPACK package [23].

THE QR-FACTORIZATION

The advantage of the singular value decomposition, in addition to giving an explicit, closed-form solution, is that it produces the singular values, which then allows one to estimate a value of the Levenberg-Marquardt parameter, by using (65) and (66), that will stabilize the solution. In addition, one can then compute exactly the condition number of the system matrix, $\overline{\overline{A}}$, by finding the ratio of the largest to smallest singular values. The disadvantage, however, is that the computation of the singular values and the matrices of singular vectors, $\overline{\overline{U}}$, $\overline{\overline{V}}$, is expensive, in terms of computer resources and time. Thus, we use another method to solve (45), or to minimize the functional, (56), and this is the QR-factorization, which we now describe, following [23].

Given that $\overline{\overline{A}}$ is $m \times n$ (where $m \geq n$), there exists a unitary matrix, $\overline{\overline{Q}}$, of order $m \times m$, such that

$$\overline{\overline{Q}}^H \overline{\overline{A}} = \begin{pmatrix} \overline{\overline{R}} \\ -- \\ \overline{\overline{0}} \end{pmatrix}, \tag{67}$$

where $\overline{\overline{R}}$ is upper triangular. If we write $\overline{\overline{Q}} = [\overline{\overline{Q}}_1, \overline{\overline{Q}}_2]$, where $\overline{\overline{Q}}_1$ has n columns, then

$$\overline{\overline{A}} = \overline{\overline{Q}}_1 \overline{\overline{R}}. \tag{68}$$

Thus, if rank $(\overline{\overline{A}}) = n$, the columns of $\overline{\overline{Q}}_1$ form an orthonormal basis for the column space of $\overline{\overline{A}}$. Now if $\overline{\overline{A}} = [\overline{\overline{A}}_1, \overline{\overline{A}}_2]$, where $\overline{\overline{A}}_1$ has k columns, and if

$$\overline{\overline{R}} = \begin{pmatrix} \overline{\overline{R}}_{11} & \overline{\overline{R}}_{12} \\ \overline{\overline{0}} & \overline{\overline{R}}_{22} \end{pmatrix}$$

where $\overline{\overline{R}}_{11}$ is $k \times k$, then

$$\overline{\overline{Q}}^H \overline{\overline{A}}_1 = \begin{pmatrix} \overline{\overline{R}}_{11} \\ -- \\ \overline{\overline{0}} \end{pmatrix}. \tag{69}$$

Hence, $\overline{\overline{Q}}$ and $\overline{\overline{R}}_{11}$ give a QR-factorization of $\overline{\overline{A}}_1$. This truncated decomposition is important for matrices whose rank is less than full, i.e., for which rank $(\overline{\overline{A}}) < \min(m, n)$.

This orthogonal triangularization is generated by Householder transformations [21,23]. Once we have this triangularization, then the solution to (48) follows:

$$\begin{aligned}
\overline{\overline{Q}}^H \overline{r} &= \overline{\overline{Q}}^H \overline{b} - \overline{\overline{Q}}^H \overline{\overline{A}} \overline{x} \\
&= \begin{pmatrix} \overline{b}_1 \\ -- \\ \overline{b}_2 \end{pmatrix} - \begin{pmatrix} \overline{\overline{R}} \\ -- \\ \overline{\overline{0}} \end{pmatrix} \overline{x} \\
&= \begin{pmatrix} \overline{b}_1 - \overline{\overline{R}} \overline{x} \\ -- \\ \overline{b}_2 \end{pmatrix}.
\end{aligned} \tag{70}$$

Since $\overline{\overline{Q}}$ is unitary, $\|\overline{\overline{Q}}^H \overline{r}\| = \|\overline{r}\|$. Thus, $\|\overline{r}\|$ is minimized when

$$\overline{r}_1 = \overline{\overline{R}} \overline{x}, \tag{71}$$

and when this is true

$$\|\overline{r}\| = \|\overline{b}_2\|. \tag{72}$$

Because $\overline{\overline{R}}$ is upper triangular the solution of (71) is easily obtained by back substitution. In solving (48) we apply the QR-factorization to the matrix $\overline{\overline{A}}$; in minimizing the functional (56), we apply the QR-factorization to the matrix of the system (59).

LINPACK [23] contains two useful subroutines, ZQRDC and ZQRSL, for solving least-squares problems by means of the QR-factorization. ZQRDC produces the QR-factorization of the matrix and passes the result to ZQRSL for the solution stage.

ANALYTIC CONTINUATION

We have already mentioned that (45) must be solved for each spatial frequency-pair, (k_x, k_y), in order to take the inverse Fourier transform of $\{\tilde{\sigma}_j\}$. The result is the conductivity distribution within the flaw, at the jth layer. Unfortunately, the matrix elements of $\overline{\overline{A}}$ become ever smaller with an increase in (k_x, k_y), thereby rendering $\overline{\overline{A}}$ so ill-conditioned that it becomes virtually impossible to get meaningful results for the lower-level conductivities within the flaw. That is, the filtering action of the Levenberg-Marquardt parameter forces $\tilde{\sigma}_j = 0$, except for the first layer or two, for large values of (k_x, k_y). Or, to put it

another way, because of the physical process of field-evanescence, which acts as a low-pass filter, the sensed magnetic field at these high spatial-frequencies is zero, so that, because of noise, one cannot use high spatial-frequencies for reconstruction by solving (45).

High-frequency components, however, are necessary for high-resolution reconstruction. Therefore, it is necessary to try to regain these missing frequencies in order to achieve the desired resolution. That this attempt at "superresolution" is feasible and practical (within limits, of course) rests upon the notion of analytic continuation [24,25]. We will state two theorems that are relevant (see [24, p. 133]):

Theorem 1. *The two-dimensional Fourier transform of a spatially bounded function is an analytic function in the (k_x, k_y)-plane.*

Theorem 2. *If any analytic function in the (k_x, k_y)-plane is known exactly in an arbitrarily small (nonzero) region of that plane, then the entire function can be found (uniquely) by means of analytic continuation.*

In order to use these theorems we recall that a flaw can be thought of as a space-limited function $g(x, y)$ (or a function with compact support). Thus, by Theorem 1, its Fourier transform, $G(u, v)$, is analytic in the (u, v)-plane. If we have only limited information about G, say, only its values at low spatial-frequencies, Theorem 2 tells us that we can uniquely extend G to the whole (u, v)-plane. Once we have continued G to the (u, v)-plane, we can take an inverse Fourier transform to recover g.

We have studied two approaches to analytic continuation, one based on direct matrix inversion via the singular value decomposition, and the other on an iterative scheme. We will discuss only the latter here.

The mathematical setting for the iterative algorithm is projections onto closed linear manifolds (CLM) in a Hilbert space [26-28]. An important feature of the method is that *a priori* knowledge about g can be incorporated into the reconstruction technique in a natural way. Such information includes the finite support and/or any constraints. In our application we know that the conductivity within the anomalous region is bounded, which in our model implies that $-1 \leq g(x, y) \leq 0$, and we also have an estimate of the support of g.

The algorithm that we used is listed here:

ALGORITHM

Let the function $G(u, v)$ be given over a prescribed region $\mathcal{L}$, and let $\mathcal{F}$ be the Fourier transform. Then starting with:

$$f_0(x, y) = \mathcal{F}^{-1}[G(u, v)];$$
$$r = 0;$$

REPEAT

$$f_r^{(1)} = P_1 f_r;$$

$$f_r^{(2)} = P_3 f_r^{(1)};$$

$$F_{r+1}^{(1)} = \mathcal{F}[f_r^{(2)}];$$

$$F_{r+1} = G + P_2 F_{r+1}^{(1)};$$

$$f_{r+1} = \mathcal{F}^{-1}[F_{r+1}];$$

$$r = r + 1;$$

UNTIL CONVERGENCE OCCURS.

The important operations in the Algorithm, in addition to the Fourier and inverse Fourier transforms, are the various projection operators P_i, which we now define:

$$P_1 f = \begin{cases} f, & (x,y) \in S, \quad S = \text{support of } f, \\ 0, & \text{otherwise.} \end{cases} \tag{73}(a)$$

$$P_2 F = \begin{cases} G(u,v), & (u,v) \in \mathcal{L}, \\ F(u,v), & (u,v) \notin \mathcal{L}, \text{ where } F(u,v) = \mathcal{F}[f(x,y)]. \end{cases} \tag{73}(b)$$

$$P_3 f = \begin{cases} -1, & \text{if } f(x,y) < -1 \\ f(x,y), & \text{if } -1 \le f(x,y) \le 0 \\ 0, & \text{if } f(x,y) > 0. \end{cases} \tag{73}(c)$$

Hence, the algorithm successively applies the known properties of the sought-for solution to the initial given data. The purpose of the theoretical analyses referred to in [26-29] is to prove that the algorithm will converge. Numerical experiments suggest various methods for speeding the convergence.

CHAPTER 7

NUMERICAL EXPERIMENTS

We have tested the theory and numerical algorithms, that were presented in the previous chapters of this report, with some numerical experiments that were performed on our computer. The model analyzed was that depicted in Figure 7, with the following data:

thickness of graphite-epoxy slab: 0.50 inches

number of layers (N_z): 10

resolution in z-direction: 0.05 inches

number of grid-points in (x,y): 64×64

resolution in (x,y)-plane: 0.05 inches

number of frequencies (N_f): 10

frequencies used (in MHz): 1, 6, 11, 16, 21, 26, 31, 36, 45, 60

The values of the electrical parameters were those stated in the second section of Chapter 2. The orientation of the current is in the y-direction, which is transverse to the fibers. The x-component of the magnetic field is assumed to be measured. Hence, we worked with the matrix, H^{xy}, as defined in (43) and (44). The frequencies that were defined above worked well with this coil-sensor orientation, in the sense that H^{xy} has a structure roughly like that shown in Figure 8, which is desirable, as we have already discussed. We are experimenting with other orientations and frequency ranges.

The flaw consists of a cylinder of square cross-section that penetrates vertically the entire thickness of the slab; i.e., the cross-section of the flaw, in each of the ten layers, is a square. The length of a side of the square is 0.15 inches. The actual flaw, at each layer, looks like Figure 9(a).

The first step in the reconstruction process was to use a program that we called RECON1. This program is our implementation of the method described in the fourth section of Chapter 6. The choice of Levenberg-Marquardt (LM) parameters was done empirically; techniques for adaptive selection of optimal LM parameters are being studied. In these experiments, the parameter values ranged between 10^{-10} and 10^{-15}. We point out that RECON1 computes the conductivities in the (k_x, k_y)-plane (Fourier space) for all (k_x, k_y). For large values of (k_x, k_y), or high spatial frequencies, the system equations become highly ill-conditioned and thus can't be expected to give accurate results for these values. However, for the small values of (k_x, k_y), or low spatial frequencies, the results are very accurate. Part of our experiment is to determine how much low frequency information must be used to produce fast, accurate reconstructions.

In Figure 9 we show the reconstructions of the flaw at each layer. These figures are labeled with the name RECON2ND which is the method of computing the inverse FFT

for all values of k_x and k_y, even those in the high range. As we can see, reconstruction is quite faithful through five layers and good from layers six through 10.

We must remember that in order to use RECON2ND, we must use RECON1 for all (k_x, k_y). An alternative is to use RECON1 to compute the unknowns for only the low frequencies, (where the system equations are not highly ill-conditioned), and then use an image-enhancement technique. The program LENTUY is our implementation of the algorithm described in the fifth section of Chapter 6.

In Figure 10, we show the reconstructions generated by simply taking the inverse FFT of the low frequency data generated by RECON1. In this case, we used $-7 \leq k_x \leq 7$ and $-7 \leq k_y \leq 7$, hence a ratio of 15 to 64. The results show that something can be detected, but the reconstruction needed to e improved. Remember, though, that we only need to produce results from RECON1 for the low frequencies and, thus, we save computing time and improve accuracy.

Figure 11 shows the results of using program LENTUY for $-7 \leq k_x \leq 7$, $-7 \leq k_y \leq 7$, and 20 iterations. Based on our previous experience with this method, we believe that the number of iterations can be reduced to 10. Also for larger flaws, the values of k_x and k_y can be reduced. We see that this method improves the resolution over INVERFFT which is to be expected and that the reconstructions are faithful through all 10 layers .

Based on these preliminary experiments and based on our previous work in image reconstructions, we are excited by the results that have been generated.

CHAPTER 8

COMMENTS AND CONCLUSIONS

The electrical model that we have developed in this report is based on a continuum description of the constitutive relations for an advanced composite material. This implies that there must be a lower limit to the resolution that can be achieved for flaw reconstruction, before the continuum hypothesis breaks down and individual fiber effects dominate. We do not know what this limit is, so we have used 0.050 inches as our resolution in the numerical experiments. Further experimental and theoretical analyses are required to better answer this question.

Fiber density directly affects the bulk longitudinal and transverse conductivities. Hence, determining (reconstructing) these conductivity values in certain anomalous regions allows us to infer the status of the fiber density within these regions; it also informs us as to the possibility of extensive fiber breakage within such regions. Hence, our model and algorithm allows us to draw conclusions about these classes of anomalies.

In some cases moisture effects can be inferred, as the following argument suggests. Transverse conduction depends upon fiber-to-fiber contact, whereas longitudinal conduction does not. One can hypothesize that as moisture is absorbed into the epoxy, the epoxy swells and reduces fiber contact [7], thereby reducing the transverse conductivity but not the longitudinal. Hence, if we can reconstruct the transverse conductivity map in an anomalous region, as well as the longitudinal conductivity map, and if the transverse map shows a significant decrease, whereas the longitudinal map does not, then we can infer that moisture is present, and that there is no significant fiber breakage, or fiber-density reduction.

This argument holds for anisotropic slabs, such as the unidirectional slab that we have considered. Fortunately, our algorithm allows us to do such a reconstruction by simply orienting the current sheet along the fiber direction, and then transverse to the fiber direction. In the discussion of Chapter 5, we will first carry out an inversion using the matrix H^{yx} and then H^{xy}.

The electromagnetic model that we have developed is quite general, in that it treats both isotropic and anisotropic slabs. In addition, it can be extended to treat anisotropic lay-ups, i.e., slabs containing layers arranged in different directions. Often, however, such slabs can be treated using a simpler isotropic theory, because the anisotropy effects are cancelled by averaging over the coarse resolution cell.

Because our model is quite general, it can account for current sources and induced currents that flow normal to the fiber plane (the z direction, in our analysis). Currents that flow in the z direction could be useful for distinguishing delaminations from other anomalies, because delaminations would tend to perturb these currents more than would other anomalies; more extensive modeling and experiments during Phase II will help clarify this question, also.

Thus, we conclude that our research effort has met the specific technical objectives,

as well as the work statement, listed in Chapter 1. Work during Phase II will include a refinement of the electromagnetic model and algorithm to account for more complex geometries, further development of numerical algorithms, development of a prototype sensor, and laboratory experiments with the prototype. All of this aims at the development of a commercial product for the wide-area inspection and quantification of advanced-composite structures.
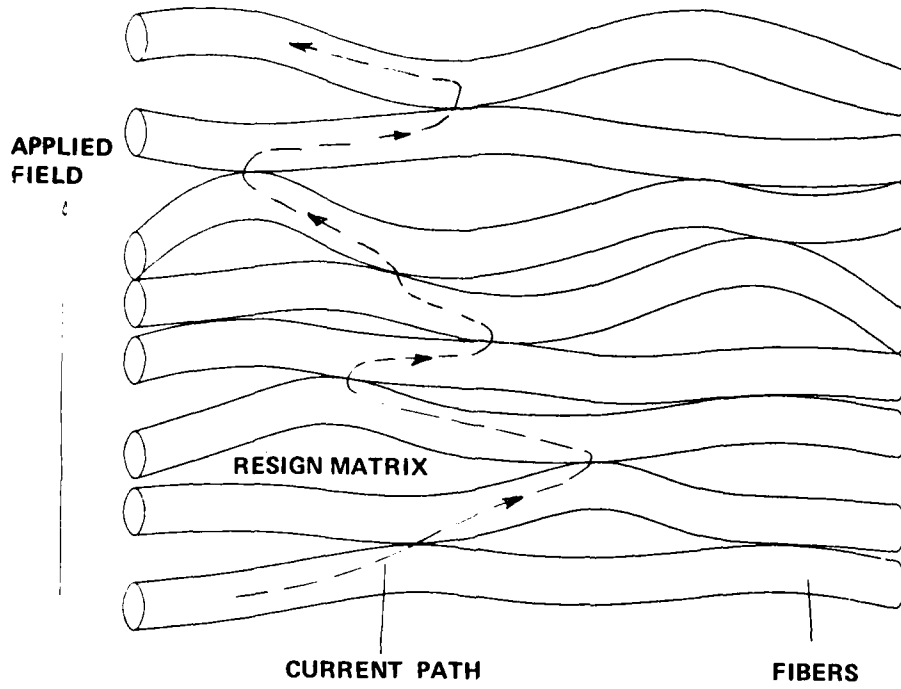
FIGURE 1. (a) HOW FIBER-TO-FIBER CONTACT ALLOWS TRANSVERSE CONDUCTION
(REFERENCE 4).
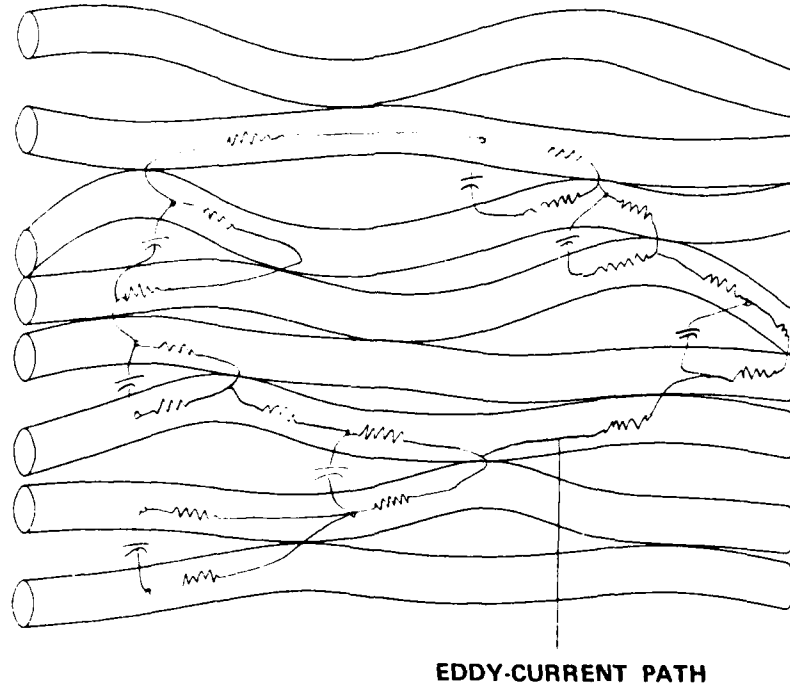
FIGURE 1. (b) A POSSIBLE AC EQUIVALENT CIRCUIT FOR EDDY-CURRENT FLAW
(REFERENCE 4).
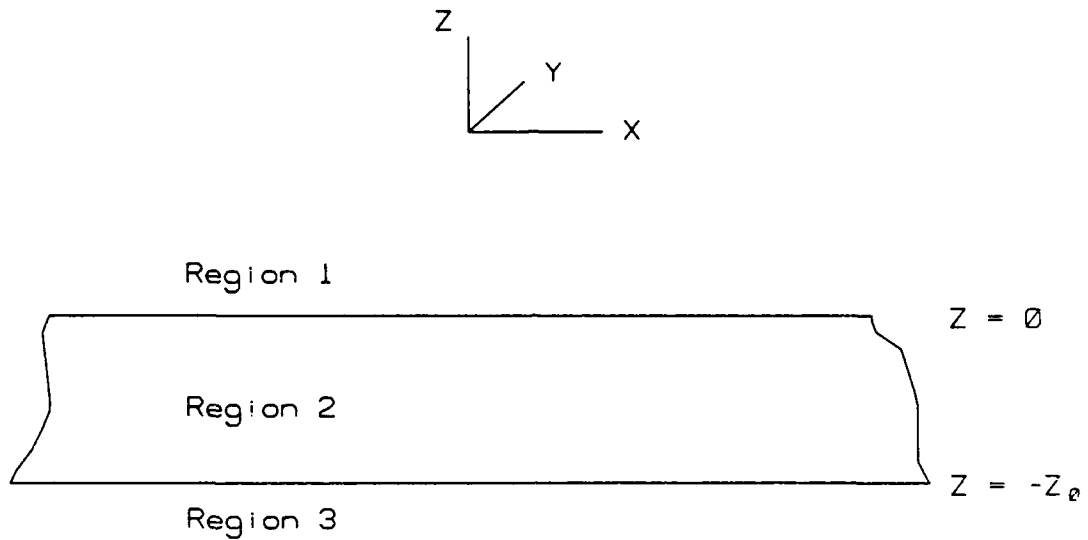
FIGURE 2. A PLANE-PARALLEL SLAB AND REGIONS DEFINED FOR COMPUTATION OF THE GREEN'S FUNCTION.
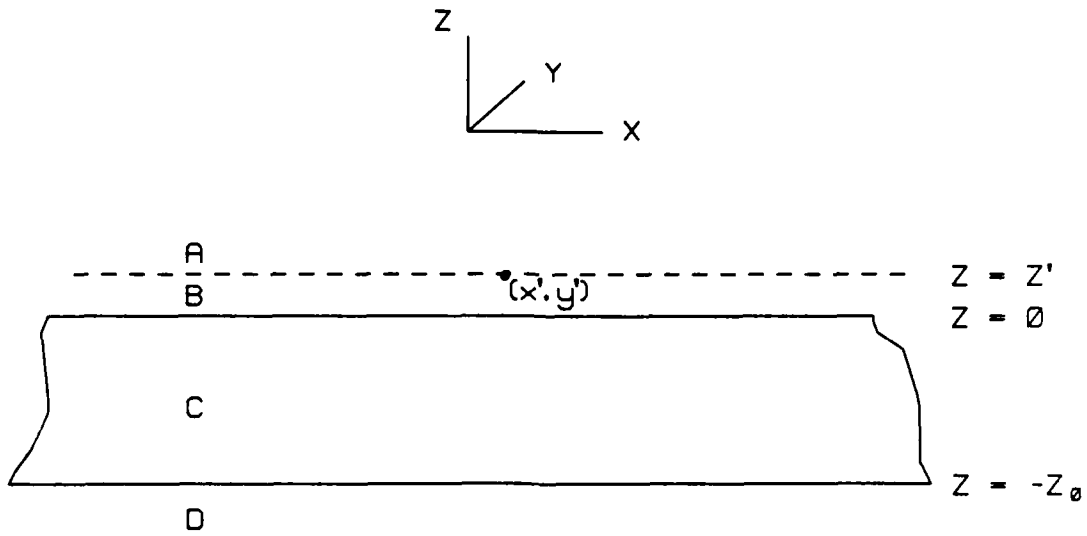
FIGURE 3. (a) A VECTOR POINT-SOURCE OF CURRENT AT (x', y', z') IN REGION 1; FOR COMPUTATION OF $\tilde{\tilde{G}}_{21}$.
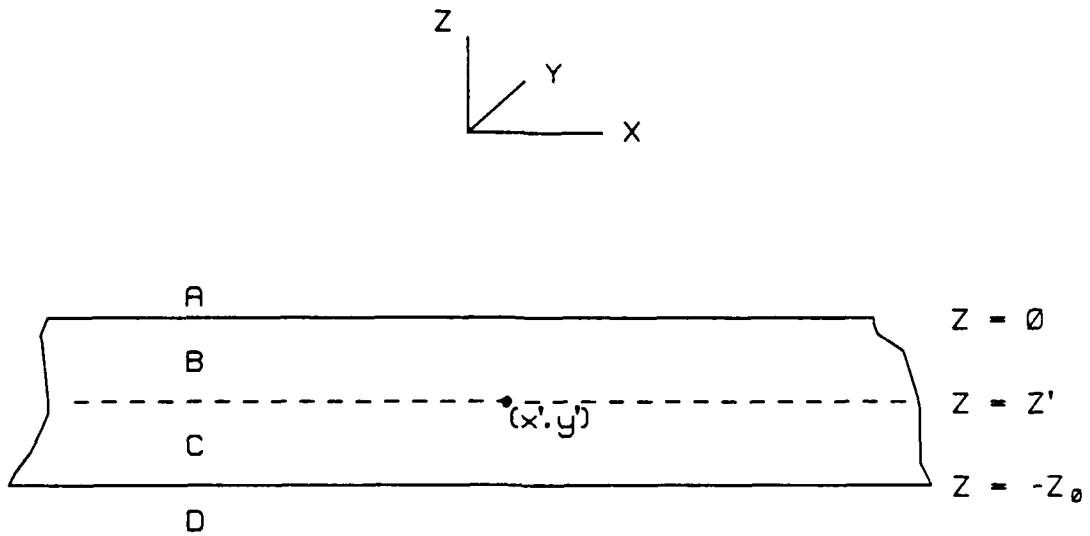
FIGURE 3. (b) A VECTOR POINT-SOURCE OF CURRENT AT (x', y', z') IN REGION 2; FOR COMPUTATION OF $\tilde{\tilde{G}}_{12}$.
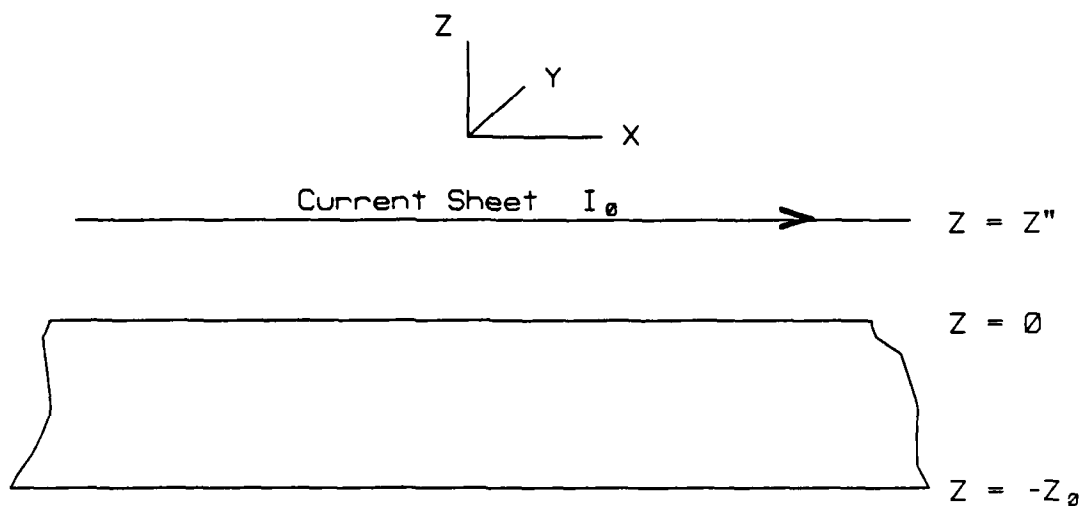
FIGURE 4. AN INFINITE CURRENT SHEET PARALLEL TO, THE ABOVE, THE ANISOTROPIC SLAB.
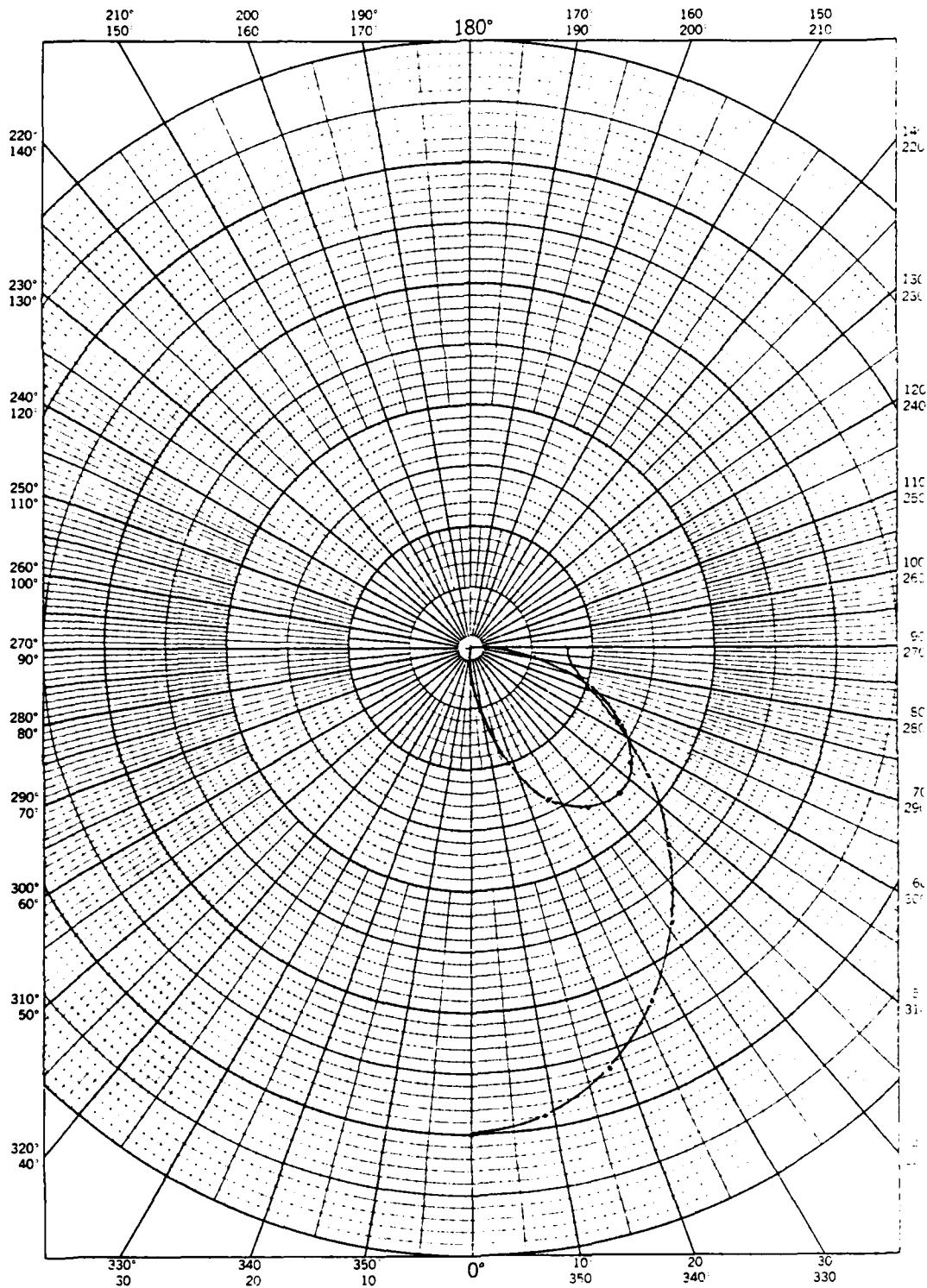
FIGURE 5. (a) VECTOR CURRENT INDUCED WITHIN ANISOTROPIC SLAB, AS A FUNCTION OF ORIENTATION OF CURRENT WITH RESPECT TO FIBERS. (THE LARGE CURVE IS THE MAGNITUDE OF THE CURRENT COMPONENT PARALLEL TO THE SHEET, AND THE SMALL CURVE IS THE MAGNITUDE OF THE CURRENT COMPONENT TRANSVERSE TO THE SHEET. FREQUENCY = 10^6 Hz; $\sigma_{11} = 2 \times 10^4$, $\sigma = 100$.)
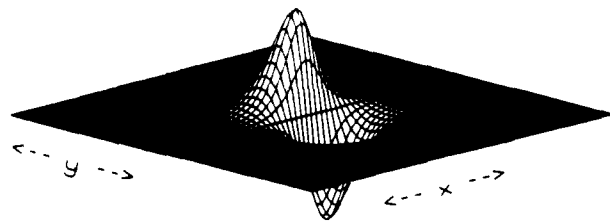
0.61973E-01

x=15.000
y=15.000

emin = -0.61973E-01

emax = 0.61973E-01

0.14119E+00

x=15.000
y=15.000

emin = -0.14119E+20

emax = 0.14119E+20

0.61973E-01

x=15.000
y=15.000

emin = -0.61973E-01
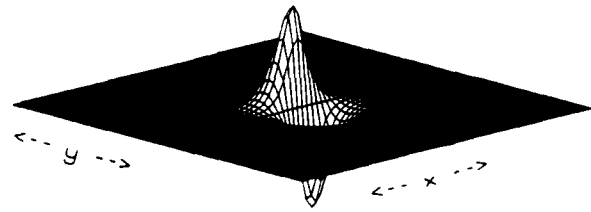
emax = 0.61973E-01

0.14119E+00

x=15.000
y=15.000

emin = -0.14119E+00

emax = 0.14119E+00

FIGURE 5. (b) ELECTRIC FIELD INDUCED INTO AN ISOTROPIC MEDIUM, BY A CIRCULAR
FILAMENTARY CURRENT LOOP, AT A DEPTH OF 0.05 IN. (FREQUENCY =
10^6 Hz; $\sigma_{11} = \sigma = 2 \times 10^4$. RE AND IM DENOTE REAL AND IMAGINARY
PARTS, RESPECTIVELY; X AND Y DENOTE x AND y COMPONENTS.)
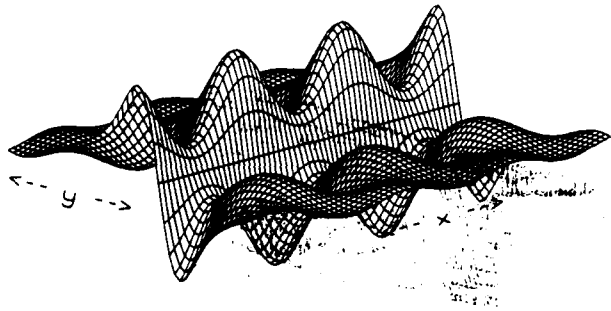
0.15169E-01

x=15.000
y=15.000

emin = -0.15169E-01

emax = 0.15169E-01
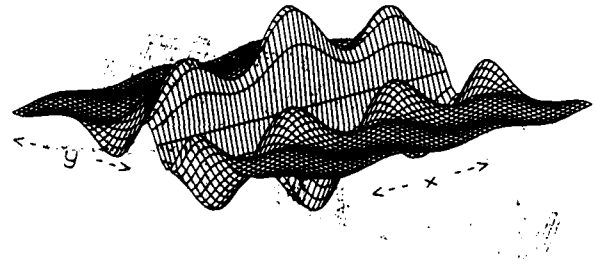
0.25104E-01

x=15.000
y=15.000

emin = -0.25104E-01

emax = 0.25104E-01
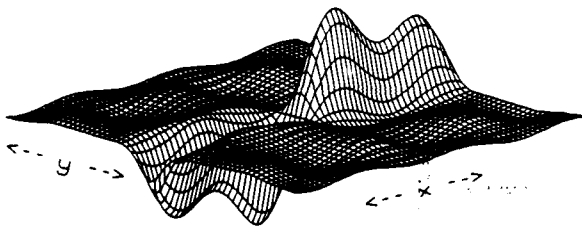
0.17900E-01

x=15.000
y=15.000

emin = -0.17900E-01

emax = 0.17900E-01
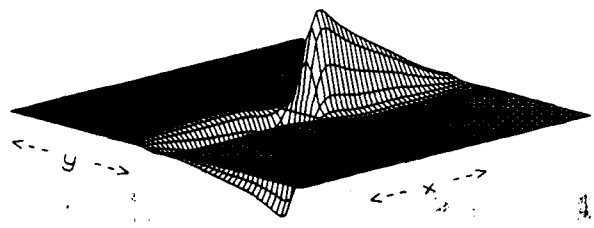
0.41955E+00

x=15.000
y=15.000

emin = -0.41955E+00

emax = 0.41955E+00

FIGURE 5. (c) ELECTRIC FIELD INDUCED INTO AN ANISOTROPIC MEDIUM, BY A CIRCULAR
FILAMENTARY CURRENT LOOP, AT A DEPTH OF 0.05 IN. (FREQUENCY = 10^6 Hz;
$\sigma_{11} = 2 \times 10^4$, $\sigma = 100$. SAME NOMENCLATURE AS FIGURE 5 (b).)
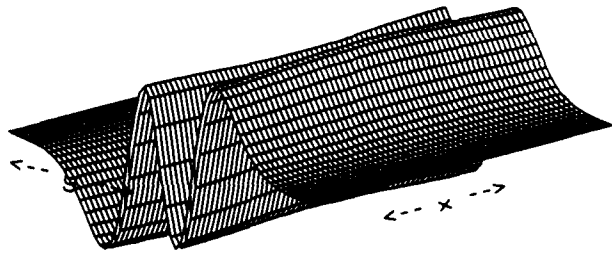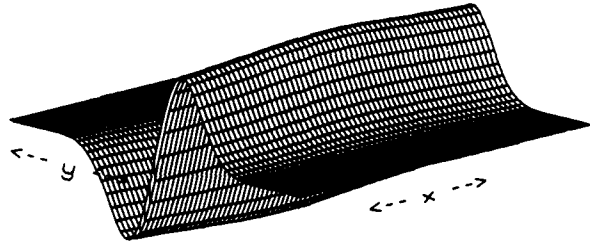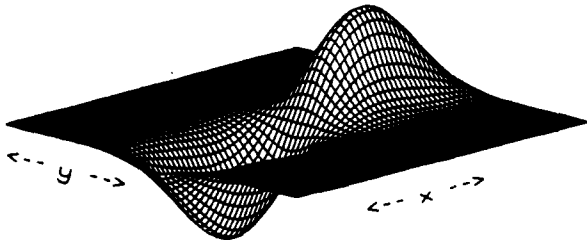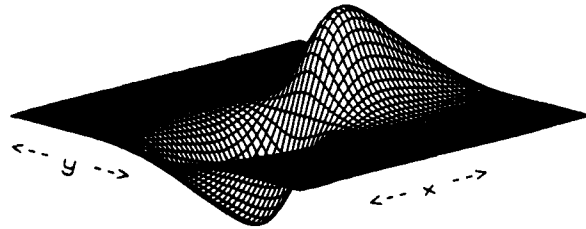
FIGURE 5. (d) SAME AS FIGURE 5 (c) EXCEPT THAT THE DEPTH IS 0.4 IN.
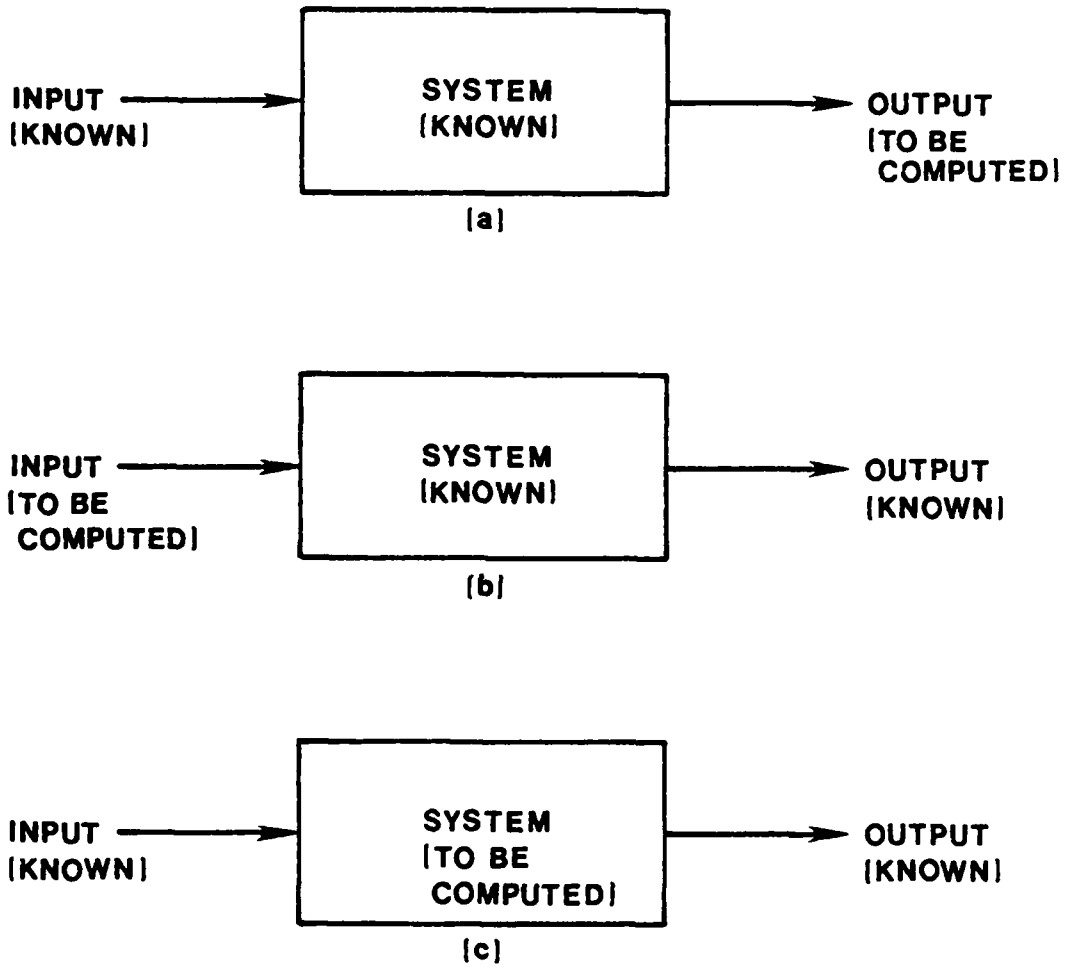
FIGURE 6. SYSTEM REPRESENTATION OF DIRECT AND INVERSE PROBLEMS.
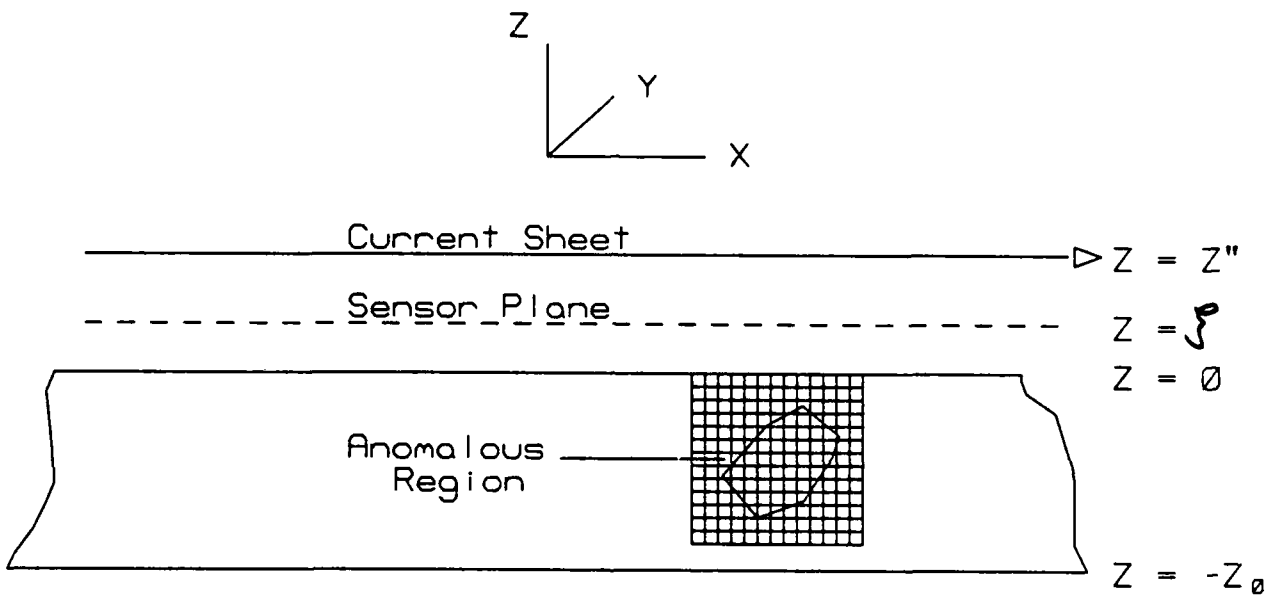
FIGURE 7. A CURRENT SHEET THAT EXCITES THE COMPOSITE WORKPIECE AND A SENSOR THAT MEASURES THE SCATTERED FIELD. THE ANOMALOUS REGION IS ENCLOSED WITHIN A MATHEMATICAL GRID.
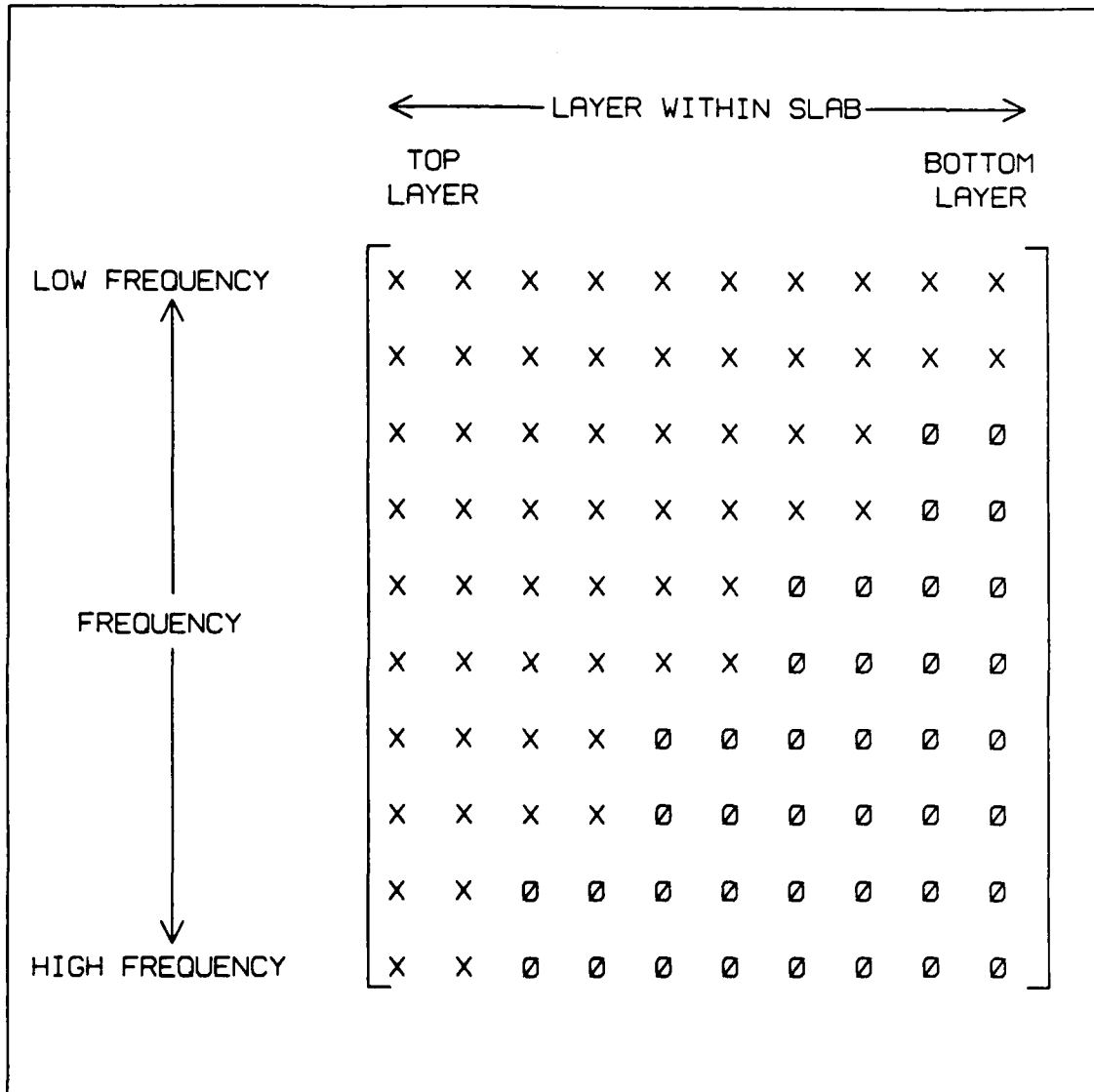
FIGURE 8. HOW THE CHOICE OF FREQUENCIES PRODUCES A RELATIVELY WELL-CONDITIONED, NEARLY TRIANGULAR SYSTEM MATRIX FOR INVERSION.

r - LEVEL	RECONSTRUCTION	r - LEVEL	RECONSTRUCTION
1		6	
2		7	
3		8	
4		9	
5		10	

FIGURE 9. THE RECONSTRUCTION OF A SQUARE, CYLINDRICAL FLAW AT EACH OF THE 10 LEVELS; USING RECON2ND.

r - LEVEL	RECONSTRUCTION	r - LEVEL	RECONSTRUCTION
1		6	
2		7	
3		8	
4		9	
5		10	

FIGURE 10. THE RECONSTRUCTION OF THE SAME FLAW; USING ONLY THE LOWEST 15 SPATIAL FREQUENCIES.
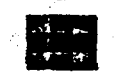
r - LEVEL	RECONSTRUCTION	r - LEVEL	RECONSTRUCTION
1		6	
2		7	
3		8	
4		9	
5		10	

FIGURE 11. THE RECONSTRUCTION OF THE SAME FLAW; APPLYING LENT-TUY ITERATION TO THE LOWEST 15 FREQUENCIES.

REFERENCES

1. Phelps, M. L., "In-Service Inspection Methods for Graphite-Epoxy Structures on Commercial Transport Aircraft," (NASA-CR-165746), Final Report (Boeing Commercial Airplan Co., Seattle).

2. Owston, C. N., "Carbon Fibre Reinforced Polymers and Non-Destructive Testing," British Journal of NDT, Vol. 15, No. 6, Jan 1973, pp. 2-11.

3. Prakash, R., and Owston, C. N., "Eddy-current Method for the Determination of Lay-up Order in Cross-plied Crfp Laminates," Composites, Vol. 7, No. 2, Apr 1976, pp. 88-92.

4. Owston, C. N., "Eddy Current Methods for the Examination of Carbon Fibre Reinforced Epoxy Resins," Materials Evaluation, Nov 1976, pp. 237-250.

5. Prakash, R., "Non-destructive Testing of Composites," Composites, Oct 1980, pp. 217-224.

6. Volpe, Vincent, "Conductivity and Electromagnetic Shielding Characteristics of Graphite/Epoxy Laminates," J. Composite Materials, Vol. 14, pp. 189-197, Jul 1980.

7. Allen, J. L., et al., "Electromagnetic Properties and Effects of Advanced Composite Materials: Measurement and Modeling," RADC-TR-78-156, Phase Report, Jun 1978 (ADA 058041).

8. Allen, J., et al., "A Technology Plan for Electromagnetic Characteristics of Advanced Composites," Rochester Institute of Technology, prepared for Rome Air Development Center, May 1976.

9. Skouby, C. D., "Electromagnetic Effects of Advanced Composites," McDonnell Aircraft Company, prepared for Office of Naval Research, Jan 1975 (ADA 010882).

10. Graf, W., Hamm, J., Nanevicz, J. E., and Tremain, D. E., "Engineering Effects of Advanced Composite Materials on Avionics," SRI International, prepared for U.S. Army Avionics R & D Command, Jul 1981 (ADA 104015).

11. Berreman, Dwight W., Journal of the Optical Society of America, Vol. 62, Number 4, Apr 1972, pp. 502-510.

12. Altman, C., and Schatzberg, A., Appl. Phys. B28, 1982, pp. 327-333.

13. Altman, C., and Schatzberg, A., Appl. Phys. B26, 1981, pp. 147-153.

14. Altman, C., Schatzberg, A., and Suchy, K., IEEE Trans. Ant. Prop., Vol. AP-32, No. 11, Nov 1984.

15. Schatzberg, A., and Altman, C., J. Plasma Physics, Vol. 26, Part 2, 1981, pp. 333-344.

16. Suchy, Kurt, and Altman, C., J. Plasma Physics, Vol. 13, Part 3, 1975, pp. 437-449.

17. Krowne, C. M., IEEE Antennas Propagation Symp. Dig., Boston, MA, Jun 25-29, 1984, pp. 569-572.

18. Krowne, C. M., IEEE Trans. Microwave Theory Tech., Vol. MTT-32, No. 12, Dec 1984, pp. 1617-1625.

19. Krowne, C. M., IEEE Trans. Ant Prop., Vol. Ap-32, No. 11, Nov 1984, pp. 1224-1230.

20. Harrington, R. F., Field Computation by Moment Methods (New York: The MacMillan Company, 1968).

21. Stewart, G. W., Introduction to Matrix Computations (New York: Academic Press, 1973).

22. Lawson, C. L., and Hanson, R. J., Solving Least Squares Problems (Englewood Cliffs: Prentice-Hall, 1974).

23. Dongarra, J. J., Bunch, J. R., Moler, C.B., and Stewart, G. W., LINPACK Users' Guide (Philadelphia: Society for Industrial and Applied Mathematics, 1979).

24. Goodman, J. W., Introduction to Fourier Optics (San Francisco: McGraw-Hill, 1968).

25. Pratt, W. K., Digital Image Processing (New York: Wiley-Interscience, 1978).

26. Youla, D. C., "Generalized Image Restoration by the Method of Alternating Orthogonal Projections," IEEE Trans. Circuits Syst., Vol. CAS-25, 1978, pp. 694-702.

27. Youla, D. C., and Webb, H., "Image Restoration by the Method of Convex Projections: Part 1-Theory," IEEE Trans. Medical Imaging, Vol. MI-1, Oct 1982, pp. 81-94.

28. Sezan, M.I., and Start, H., "Image Restoration by the Method of Convex Projections: Part 2-Applications and Numerical Results," EEE Trans. Medical Imaging, Vol. MI-1, Oct 1982, pp. 95-101.

29. Lent, A., and Tuy, H., "An Iterative Method for the Extrapolation of Band Limited Functions," J. Math. Anal. Appl., Vol. 83, 1981, pp. 554-565.

30. Sabbagh, L. David, and Sabbagh, Harold A., "Development of a System to Invert Eddy-Current Data and Reconstruct Flaws," in D. O. Thompson and D. E. Chimenti, eds., Review of Progress in Quantitative Nondestructive Evaluation, Vol. 2B (New York: Plenum Press, 1983).

31. Sabbagh, Harold A., and Sabbagh, L. David, "Experimental Verification of an Inversion Algorithm for Flaw Characterization Using Eddy-Currents," in Thompson, D. O., and Chimenti, D. E., eds., Review of Progress in Quantitative Nondestructive Evaluation, Vol. 3A (New York: Plenum Press, 1984).

APPENDIX A

EIGENMODE ANALYSIS OF ANISOTROPIC MEDIA

Start with the homogeneous form of (11), i.e., with $\tilde{\bar{j}}^{(i)} = 0$. Since the matrix, $\overline{\overline{S}}$, is constant with respect to z for a nonstratified medium, we look for eigenvector solutions of the form:

$$\tilde{e}_t(z) = \tilde{\bar{e}}_0 \exp(\lambda z), \qquad (A1)$$

where $\tilde{\bar{e}}_0$ is a constant vector, and λ is a parameter to be determined. Upon substituting (A1) into (11), we get the eigenvalue problem:

$$\overline{\overline{S}}\, \tilde{\bar{e}}_0 = \lambda \tilde{\bar{e}}_0. \qquad (A2)$$

The eigenvalues are the solutions of the secular equation

$$\det\left[\overline{\overline{S}} - \lambda \overline{\overline{I}}\right] = 0. \qquad (A3)$$

There will be four eigenvalues, and the eigenvector corresponding to each eigenvalue can be computed from the two independent equations arising out of the four simultaneous equations in (A2).

In the principal coordinate system, the generalized permittivity tensor, $\bar{\bar{\epsilon}}$, is diagonal, as in (1). Hence, the only nonzero K_{ij} in (13) are $K_{11} \neq K_{22} = K_{33}$. Upon letting $K_{22} = K_{33} = K$, we get:

$$S_{13} = -j\frac{k_x k_y}{\omega K}, \qquad S_{14} = -j\omega\mu_0 + j\frac{k_x^2}{\omega K}, \quad S_{23} = j\omega\mu_0 - j\frac{k_y^2}{\omega K},$$

$$S_{24} = j\frac{k_x k_y}{\omega K}, \qquad S_{31} = j\frac{k_x k_y}{\omega\mu_0}, \qquad S_{32} = j\omega K - j\frac{k_x^2}{\omega\mu_0}, \qquad (A4)$$

$$S_{41} = -j\omega K_{11} + j\frac{k_y^2}{\omega\mu_0}, \quad S_{42} = -j\frac{k_x k_y}{\omega\mu_0}.$$

When these coefficients are substituted into (A3), and the determinant expanded, we obtain a quartic equation for λ:

$$\lambda^4 - a\lambda^2 + b = 0, \qquad (A5)$$

where

$$a = -\omega^2\mu_0(K + K_{11}) + 2k_y^2 + k_x^2(1 + K_{11}/K)$$

$$b = \omega^4\mu_0^2 K K_{11} - \omega^2\mu_0(2K_{11}k_x^2 + (K + K_{11})k_y^2) \qquad (A6)$$

$$+ k_x^2 k_y^2(1 + K_{11}/K) + k_x^4(K_{11}/K) + k_y^4.$$

Hence, the eigenvalues (the roots of (A5)) are:

$$\pm\lambda_1 = \pm j(\omega^2\mu_0 K_{11} - (K_{11}/K)k_x^2 - k_y^2)^{1/2}$$

$$\pm\lambda_3 = \pm j(\omega^2\mu_0 K - k_x^2 - k_y^2)^{1/2}. \qquad (A7)$$

Note that λ_3 corresponds to an isotropic medium, and that the anisotropy is manifest in λ_1. Clearly, if $K_{11} = K$, then $\lambda_1 = \lambda_3$, which agrees with the results for an isotropic medium.

Corresponding to each eigenvalue, λ, is an eigenvector that satisfies (A2). We have some liberty in choosing the two independent equations that generate the eigenvectors; hence, there is some arbitrariness in choosing the eigenvectors. We choose the following:

$$\bar{v}_1 = \begin{pmatrix} S_{14}/\lambda_1 \\ S_{24}/\lambda_1 \\ 0 \\ 1 \end{pmatrix}, \ \bar{v}_2 = \begin{pmatrix} -S_{14}/\lambda_1 \\ -S_{24}/\lambda_1 \\ 0 \\ 1 \end{pmatrix}, \ \bar{v}_3 = \begin{pmatrix} 0 \\ \lambda_3/S_{32} \\ 1 \\ -S_{31}/S_{32} \end{pmatrix}, \ \bar{v}_4 = \begin{pmatrix} 0 \\ -\lambda_3/S_{32} \\ 1 \\ -S_{31}/S_{32} \end{pmatrix} . \quad (A8)$$
$$(+\lambda_1) \qquad\qquad (-\lambda_1) \qquad\qquad (+\lambda_3) \qquad\qquad (-\lambda_3)$$

The second and fourth vectors are the two $(+)$-going modes, and the first and third are the two $(-)$-going modes, in the z-direction.

These results are used in computing the Green's function in Chapter 3.

APPENDIX B

COMPUTATION OF COEFFICIENTS FOR $\widetilde{\widetilde{\overline{G}}}_{12}$

In this appendix we want to fill in a few of the steps outlined in Section III for $\widetilde{\widetilde{\overline{G}}}_{12}$. The computations for $\widetilde{\widetilde{\overline{G}}}_{21}$ are similar.

Referring to Figure 3(b), together with (21), we have for the boundary conditions at $z = 0$ and $z = -z_0$:

$$a \begin{pmatrix} -\alpha_{10} \\ -\alpha_{20} \\ 0 \\ 1 \end{pmatrix} + b \begin{pmatrix} 0 \\ -\beta_{10} \\ 1 \\ -\beta_{20} \end{pmatrix} = c \begin{pmatrix} \alpha_1 \\ \alpha_2 \\ 0 \\ 1 \end{pmatrix} e^{\lambda_1 z'} + d \begin{pmatrix} -\alpha_1 \\ -\alpha_2 \\ 0 \\ 1 \end{pmatrix} e^{-\lambda_1 z'}$$

$$+ e \begin{pmatrix} 0 \\ \beta_1 \\ 1 \\ -\beta_2 \end{pmatrix} e^{\lambda_3 z'} + f \begin{pmatrix} 0 \\ -\beta_1 \\ 1 \\ -\beta_2 \end{pmatrix} e^{-\lambda_3 z'}; \quad (B1)(a)$$

$$c' \begin{pmatrix} \alpha_1 \\ \alpha_2 \\ 0 \\ 1 \end{pmatrix} e^{\lambda_1 (z' - z_0)} + d' \begin{pmatrix} -\alpha_1 \\ -\alpha_2 \\ 0 \\ 1 \end{pmatrix} e^{-\lambda_1 (z' - z_0)}$$

$$+ e' \begin{pmatrix} 0 \\ \beta_1 \\ 1 \\ -\beta_2 \end{pmatrix} e^{\lambda_3 (z' - z_0)} + f' \begin{pmatrix} 0 \\ -\beta_1 \\ 1 \\ -\beta_2 \end{pmatrix} e^{-\lambda_3 (z' - z_0)} = g \begin{pmatrix} \alpha_{10} \\ \alpha_{20} \\ 0 \\ 1 \end{pmatrix} + h \begin{pmatrix} 0 \\ \beta_{10} \\ 1 \\ -\beta_{20} \end{pmatrix}. \quad (B1)(b)$$

The boundary condition at $z = z'$ is the discontinuity induced by the point current-source. For an x-directed current the equation is:

$$c \begin{pmatrix} \alpha_1 \\ \alpha_2 \\ 0 \\ 1 \end{pmatrix} + d \begin{pmatrix} -\alpha_1 \\ -\alpha_2 \\ 0 \\ 1 \end{pmatrix} + e \begin{pmatrix} 0 \\ \beta_1 \\ 1 \\ -\beta_2 \end{pmatrix} + f \begin{pmatrix} 0 \\ -\beta_1 \\ 1 \\ -\beta_2 \end{pmatrix}$$

$$= c' \begin{pmatrix} \alpha_1 \\ \alpha_2 \\ 0 \\ 1 \end{pmatrix} + d' \begin{pmatrix} -\alpha_1 \\ -\alpha_2 \\ 0 \\ 1 \end{pmatrix} + e' \begin{pmatrix} 0 \\ \beta_1 \\ 1 \\ -\beta_2 \end{pmatrix} + f' \begin{pmatrix} 0 \\ -\beta_1 \\ 1 \\ -\beta_2 \end{pmatrix} - \begin{pmatrix} 0 \\ 0 \\ 0 \\ 1 \end{pmatrix}, \quad (B2)(a)$$

and for the y-directed current it is:

$$c \begin{pmatrix} \alpha_1 \\ \alpha_2 \\ 0 \\ 1 \end{pmatrix} + d \begin{pmatrix} -\alpha_1 \\ -\alpha_2 \\ 0 \\ 1 \end{pmatrix} + e \begin{pmatrix} 0 \\ \beta_1 \\ 1 \\ -\beta_2 \end{pmatrix} + f \begin{pmatrix} 0 \\ -\beta_1 \\ 1 \\ -\beta_2 \end{pmatrix}$$

$$= c' \begin{pmatrix} \alpha_1 \\ \alpha_2 \\ 0 \\ 1 \end{pmatrix} + d' \begin{pmatrix} -\alpha_1 \\ -\alpha_2 \\ 0 \\ 1 \end{pmatrix} + e' \begin{pmatrix} 0 \\ \beta_1 \\ 1 \\ -\beta_2 \end{pmatrix} + f' \begin{pmatrix} 0 \\ -\beta_1 \\ 1 \\ -\beta_2 \end{pmatrix} + \begin{pmatrix} 0 \\ 0 \\ 1 \\ 0 \end{pmatrix} . \quad (B2)(b)$$

Because the boundary conditions at $z = 0$ and $z = z'$ are independent of current direction, it is best to work with them first and solve for $(c - f)$ in terms of (a, b), using (B1)(a), and $(c' - f')$ in terms of (g, h), using (B1)(b). The results, after some straightforward algebra, are:

$$c = \frac{a(\alpha_1 - \alpha_{10}) + b\alpha_1(\beta_2 - \beta_{20})}{2\alpha_1} e^{-\lambda_1 z'}$$

$$d = \frac{a(\alpha_1 + \alpha_{10}) + b\alpha_1(\beta_2 - \beta_{20})}{2\alpha_1} e^{\lambda_1 z'}$$

$$e = \frac{a\left(\frac{\alpha_2\alpha_{10} - \alpha_1\alpha_{20}}{\alpha_1}\right) + b(\beta_1 - \beta_{10})}{2\beta_1} e^{-\lambda_3 z'}$$

$$f = \frac{-a\left(\frac{\alpha_2\alpha_{10} - \alpha_1\alpha_{20}}{\alpha_1}\right) + b(\beta_1 + \beta_{10})}{2\beta_1} e^{\lambda_3 z'}, \qquad (B3)(a)$$

$$c' = \frac{g(\alpha_1 + \alpha_{10}) + h\alpha_1(\beta_2 - \beta_{20})}{2\alpha_1} e^{-\lambda_1(z' - z_0)}$$

$$d' = \frac{g(\alpha_1 - \alpha_{10}) + h\alpha_1(\beta_2 - \beta_{20})}{2\alpha_1} e^{\lambda_1(z' - z_0)}$$

$$e' = \frac{g\left(\frac{\alpha_1\alpha_{20} - \alpha_2\alpha_{10}}{\alpha_1}\right) + h(\beta_1 + \beta_{10})}{2\beta_1} e^{-\lambda_3(z' - z_0)}$$

$$f' = \frac{-g\left(\frac{\alpha_1\alpha_{20} - \alpha_2\alpha_{10}}{\alpha_1}\right) + h(\beta_1 + \beta_{10})}{2\beta_1} e^{\lambda_3(z' - z_0)}. \qquad (B3)(b)$$

Now we substitute these expressions into the remaining boundary condition at $z = z'$, for either the x- or y-directed current source. For the x-directed source:

$$(c - c') \begin{pmatrix} \alpha_1 \\ \alpha_2 \\ 0 \\ 1 \end{pmatrix} + (d - d') \begin{pmatrix} -\alpha_1 \\ -\alpha_2 \\ 0 \\ 1 \end{pmatrix} + (e - e') \begin{pmatrix} 0 \\ \beta_1 \\ 1 \\ -\beta_2 \end{pmatrix} + (f - f') \begin{pmatrix} 0 \\ -\beta_1 \\ 1 \\ -\beta_2 \end{pmatrix} = \begin{pmatrix} 0 \\ 0 \\ 0 \\ -1 \end{pmatrix}, (B4)(a)$$

and for the y-directed source:

$$(c - c') \begin{pmatrix} \alpha_1 \\ \alpha_2 \\ 0 \\ 1 \end{pmatrix} + (d - d') \begin{pmatrix} -\alpha_1 \\ -\alpha_2 \\ 0 \\ 1 \end{pmatrix} + (e - e') \begin{pmatrix} 0 \\ \beta_1 \\ 1 \\ -\beta_2 \end{pmatrix} + (f - f') \begin{pmatrix} 0 \\ -\beta_1 \\ 1 \\ -\beta_2 \end{pmatrix} = \begin{pmatrix} 0 \\ 0 \\ 1 \\ 0 \end{pmatrix}. (B4)(b)$$

The solutions of these equations are:

x-directed source:

$$(c - c') = -1/2, \quad (d - d') = -1/2, \quad (e - e') = 0, \quad (f - f') = 0; \qquad (B5)(a)$$

y-directed source:

$$(c - c') = \beta_2/2, \quad (d - d') = \beta_2/2, \quad (e - e') = 1/2, \quad (f - f') = 1/2. \qquad (B5)(b)$$

Upon using (B3), we eliminate $(c - f), (c' - f')$, in favor of (a, b, g, h):

$$a(\alpha_1 - \alpha_{10}) + b\alpha_1(\beta_2 - \beta_{20}) - g(\alpha_1 + \alpha_{10})e^{\lambda_1 z_0} - h\alpha_1(\beta_2 - \beta_{20})e^{\lambda_1 z_0} = v_1 \qquad (B6)(a)$$

$$a(\alpha_1 + \alpha_{10}) + b\alpha_1(\beta_2 - \beta_{20}) - g(\alpha_1 - \alpha_{10})e^{-\lambda_1 z_0} - h\alpha_1(\beta_2 - \beta_{20})e^{-\lambda_1 z_0} = v_2 \qquad (B6)(b)$$

$$a\left(\frac{\alpha_2\alpha_{10} - \alpha_1\alpha_{20}}{\alpha_1}\right) + b(\beta_1 - \beta_{10}) - g\left(\frac{\alpha_1\alpha_{20} - \alpha_2\alpha_{10}}{\alpha_1}\right)e^{\lambda_3 z_0}$$
$$- h(\beta_1 + \beta_{10})e^{\lambda_3 z_0} = v_3 \quad (B6)(c)$$

$$-a\left(\frac{\alpha_2\alpha_{10} - \alpha_1\alpha_{20}}{\alpha_1}\right) + b(\beta_1 + \beta_{10}) + g\left(\frac{\alpha_1\alpha_{20} - \alpha_2\alpha_{10}}{\alpha_1}\right)e^{-\lambda_3 z_0}$$
$$- h(\beta_1 - \beta_{10})e^{-\lambda_3 z_0} = v_4, \quad (B6)(d)$$

where the vector on the right side is given by

$$\begin{pmatrix} -\alpha_1 e^{\lambda_1 z'} \\ -\alpha_1 e^{-\lambda_1 z'} \\ 0 \\ 0 \end{pmatrix}, \text{for x-directed source;} \qquad (B7)(a)$$

$$\begin{pmatrix} \alpha_1\beta_2 e^{\lambda_1 z'} \\ \alpha_1\beta_2 e^{-\lambda_1 z'} \\ \beta_1 e^{\lambda_3 z'} \\ \beta_1 e^{-\lambda_3 z'} \end{pmatrix}, \text{for y-directed source.} \qquad (B7)(b)$$

(B6) and (B7) are the final analytic expressions; (a, b, g, h) are computed numerically, and the results used in the Green's function. Note that we have not used the exponential term, $e^{j(k_x x' + k_y y')}$, that appears in (19) and (20). This is due to the fact that in computing the transverse Fourier transform of the Green's function, as defined in (15), we must divide by $\tilde{j}^{(i)}$, which is the exponential term.

APPENDIX C

COMPUTATION OF $\bar{\tilde{j}}^{(i)}$ FOR CIRCULAR CURRENT SHEETS

If the sheet lies in the plane $z = z''$, and has a coil-turns density of $f(r)$, where r is the radial coordinate, then the current density is given by

$$\overline{J}^{(i)}(x,y,z) = I_0 \delta(z - z'')(-\bar{a}_x \sin\theta + \bar{a}_y \cos\theta)f(r), \qquad (C1)$$

where I_0 is the total current carried by the coil. Then

$$\bar{\tilde{j}}^{(i)}(k_x, k_y, z) = \frac{I_0 \delta(z - z'')}{4\pi^2} \iint_{-\infty}^{\infty} (-\bar{a}_x \sin\theta + \bar{a}_y \cos\theta)f(r)e^{j(k_x x + k_y y)}\,dx\,dy. \qquad (C2)$$

Upon transforming to cylindrical coordinates:

$$\begin{aligned}
\bar{\tilde{j}}^{(i)}(k_x, k_y, z) &= \frac{I_0 \delta(z - z'')}{4\pi^2} \int_0^{2\pi} d\theta \int_0^{\infty} rf(r)(-\bar{a}_x \sin\theta + \bar{a}_y \cos\theta)e^{jr(k_x \cos\theta + k_y \sin\theta)}\,dr \\
&= \frac{I_0 \delta(z - z'')}{4\pi^2} \int_0^{\infty} f(r)\left[\int_0^{2\pi} r(-\bar{a}_x \sin\theta + \bar{a}_y \cos\theta)e^{jr(k_x \cos\theta + k_y \sin\theta)}\,d\theta\right]dr \\
&= \frac{-jI_0 \delta(z - z'')}{4\pi^2} \int_0^{\infty} f(r)\left[\left(-\bar{a}_x \frac{d}{dk_y} + \bar{a}_y \frac{d}{dk_x}\right)\int_0^{2\pi} e^{jr(k_x \cos\theta + k_y \sin\theta)}\,d\theta\right]dr.
\end{aligned}$$
$$(C3)$$

The θ-integral can be easily calculated by first transforming into cylindrical coordinates in Fourier-space:

$$\begin{aligned}
k_x &= k_r \cos\phi \\
k_y &= k_r \sin\phi \\
k_r &= (k_x^2 + k_y^2)^{1/2}.
\end{aligned} \qquad (C4)$$

Thus, the integrand becomes $e^{jk_r r \cos(\theta - \phi)}$, which, according to a well-known identity involving Bessel functions, is

$$e^{jk_r r \cos(\theta - \phi)} = J_0(k_r r) + 2\sum_{k=1}^{\infty} j^k J_k(k_r r)\cos k(\theta - \phi). \qquad (C5)$$

Only the first term survives the integral over 2π radians, so that (C3) becomes

$$\begin{aligned}
\bar{\tilde{j}}^{(i)}(k_x, k_y, z) &= \frac{-jI_0 \delta(z - z'')}{2\pi}\left(-\bar{a}_x \frac{d}{dk_y} + \bar{a}_y \frac{d}{dk_x}\right)\int_0^{\infty} f(r)J_0(k_r r) \\
&= \frac{jI_0 \delta(z - z'')}{2\pi}\left(-\bar{a}_x \frac{k_y}{k_r} + \bar{a}_y \frac{k_x}{k_r}\right)\int_0^{\infty} rf(r)J_1(k_r r)\,dr.
\end{aligned} \qquad (C6)$$

C-1

The final integral is the Bessel transform of the coil-turns density, $f(r)$. This transform can be easily computed for a number of interesting practical coil configurations. For example, if the coil consists of a single filamentary loop of radius r_0, then $f(r) = \delta(r - r_0)$, so that the Bessel transform is simply $r_0 J_1(k_r r_0)$. Hence,

$$\bar{\bar{j}}^{(i)} = \frac{j I_0 r_0 \delta(z - z'')}{2\pi} J_1(k_r r_0) \left(-\bar{a}_x \frac{k_y}{k_r} + \bar{a}_y \frac{k_x}{k_r} \right). \qquad (C7)$$

For a coil with a uniform distribution of turns, whose density is N_c, and extends to a radius of r_0, the Bessel transform reduces to $N_c \int_0^{r_0} r J_1(k_r r) dr$, which can only be computed numerically. Therefore, for such a coil

$$\bar{\bar{j}}^{(i)} = \frac{j N_c I_0 \delta(z - z'')}{2\pi} \left(-\bar{a}_x \frac{k_y}{k_r} + \bar{a}_y \frac{k_x}{k_r} \right) \int_0^{r_0} r J_1(k_r r) dr. \qquad (C8)$$

Finally, for a coil of radius r_0, whose density of turns linearly increases, i.e., for which $f(r) = N_c r$, the Bessel transform can be explicitly computed, with the result that

$$\bar{\bar{j}}^{(i)} = \frac{j N_c r_0^3 I_0 \delta(z - z'')}{2\pi} \left(-\bar{a}_x \frac{k_y}{k_r} + \bar{a}_y \frac{k_x}{k_r} \right) \left(\frac{J_2(k_r r_0)}{k_r r_0} \right). \qquad (C9)$$

C-2

DISTRIBUTION

	Copies		Copies
Director Strategic Systems Project Office ATTN: SP 2015 Washington, DC 20376-5002	1	Lawrence Livermore Laboratory ATTN: Edmund K. Miller University of California P. O. Box 5504 Livermore, CA 94550	1
Defense Technical Information Cntr Cameron Station Alexandria, VA 22314	12	LTV Steel Company ATTN: Herbert Schilling Research Center	1
Library of Congress Attn: Gift & Exchange Div. Washington, DC 20540	4	6801 Brecksville Road Independence, OH 55141	
U.S. Department of Energy ATTN: Charles Horace Craig Forrestal Bldg., CE-131 Washington, DC 20585	1	Texas Research Institute, Inc. ATTN: Cecil M. Teller 9063 Bee Caves Road Austin, TX 78746	1

University of Surrey
ATTN: John R. Bowler
      Physics Department
Gildford
Surrey, United Kingdom
	1	Electronic and Electrical
		  Engineering Department
		University College London
		ATTN: Leonard J. Bond
		Torrington Place WC1E7Je
			1

Oak Ridge National Laboratory Nuclear Division ATTN: Caius V. Dodd P. O. Box X Oak Ridge, TN 37830	1	Dresser Atlas ATTN: Samuel G. Marinov 10201 Westheimer Houston, TX 77042	1

Southwest Research Institute
ATTN: James E. Doherty
      G. P. Singh
6220 Culebra Road
San Antonio, TX 78284
	1
	1
		Electric Power Research Inst.
		ATTN: Gary J. Dau
		      Michael J. Avioli, Jr.
		3412 Hillview Avenue
		Palo Alto, CA 94303
			1
			1

Martin Marietta Aerospace ATTN: Ward D. Rummel, P.E. P. O. Box 179 Denver, CO 80201	1	Magnaflux Corporation ATTN: Donald Yuhas 2301 Arthur Avenue Elk Grove Village, IL 60007	1

(1)

	Copies		Copies
United States Steel Corp. ATTN: Michael L. Mester 125 Jamison Lane Monroeville, PA 15146	1	Purdue University ATTN: John Nyenhuis School of Electrical Eng. West Lafayette, IN 47907	1
Qualcorp ATTN: Parker E. Moreland, Jr. Shelter Rock Road Danbury, CT 06810	1	Indiana University ATTN: Roger Newton Physics Department Gloomington, IN 47405	1
Fokker B.V. ATTN: K. J. Rienks P. O. Box 7600 1117 ZJ Shiphol The Netherlands	1	Sabbagh Associates, Inc. 2634 Round Hill Lane Bloomington, IN 47401	10

Internal Distribution

	Copies
R	1
R03	1
R30	1
R3C1	1
R31	1
S22 (J. Trader)	1
S20	1
R34	1
R34 (S. N. Vernon)	1
E232	3
E231	9

United Technologies Res. Center
ATTN: Richard Williams   1
      Robert Reed   1
Mail Stop 86
East Hartford, CT 06108

Corporation for Science and
  Technology
ATTN: John D. Hague, Pres.   1
One North Capitol Avenue
Indianapolis, IN 46204

Magna Sonics
ATTN: George A. Alers, Pres. 1
215 Sierra Drive, SE
Albuquerque, NM 87108

Nortec Corporation
ATTN: C. L. Frederick   1
421 North Quay
Kennewick, WA 99336

LTV Aerospace & Defense Company
ATTN: Tony Hamilton   1
Vought Aero Products Division
P. O. Box 225907
Dallas, TX 75265

Morton Thiokol, Inc.
ATTN: D. P. Lappas   1
Wasatch Operations, Strategic Div.
P. O. Box 524 M/S 731
Brigham City, UT 84302